Gas-phase-dependent properties of SnO_2 (110), (100), and (101) single-crystal surfaces: Structure, composition, and electronic properties

Matthias Batzill, Khabibulakh Katsiev, James M. Burst, and Ulrike Diebold
Department of Physics, Tulane University, New Orleans, Louisiana 70118, USA

Anne M. Chaka
Chemical Science and Technology Laboratory, National Institute of Standards, Gaithersburg, Maryland 20899-8380, USA

Bernard Delley
Paul Scherrer Institut, Villigen, Switzerland

(Received 19 March 2005; revised manuscript received 23 June 2005; published 14 October 2005)

The dependence of the surface structure, composition, and electronic properties of three low index SnO_2 surfaces on the annealing temperature in vacuum has been investigated experimentally by low energy He^+ ion scattering spectroscopy (LEIS), low energy electron diffraction (LEED), scanning tunneling microscopy (STM), and angle resolved valence band photoemission (ARUPS) using synchrotron radiation. Transitions from stoichiometric to reduced surface phases have been observed at 440–520 K, 610–660 K, and 560–660 K for the SnO_2 (110), (100), and (101) surfaces, respectively. Density functional theory has been employed to assess the oxidation state and stability of different surface structures and compositions at various oxygen chemical potentials. The reduction of the SnO_2 surfaces is facilitated by the dual valency of Sn, and for all three surfaces a transition from Sn(IV) to Sn(II) is observed. For the (100) and (101) surfaces, theory supports the experimental observations that the phase transitions are accomplished by removal of bridging oxygen atoms from a stoichiometric SnO_2 surface, leaving a SnO surface layer with a 1×1 periodicity. For the (110) surface the lowest energy surface under reducing conditions was predicted for a model with a SnO surface layer with all bridging oxygen and every second row of in-plane oxygen atoms removed. *Ab initio* atomistic thermodynamic calculations predict the phase transition conditions for the (101) surface, but there are significant differences with the experimentally observed transition temperatures for the (110) and (100) surfaces. This discrepancy between experiment and thermodynamic equilibrium calculations is likely because of a dominant role of kinetic processes in the experiment. The reduction of surface Sn atoms from a Sn(IV) to a Sn(II) valence state results in filling of the Sn-5*s* states and, consequently, the formation of Sn derived surface states for all three investigated surfaces. The dispersion of the surface states for the reduced (101) surface was determined and found to be in good agreement with the DFT results. For the (110) surface, the 4×1 reconstruction that forms after sputter and annealing cycles was also investigated. For this surface, states that span almost the entire band gap were observed. Resonant photoemission spectroscopy identified all the surface states on the reduced SnO_2 surfaces as Sn derived.

DOI: 10.1103/PhysRevB.72.165414 PACS number(s): 68.47.Gh, 68.35.Bs, 68.35.Md, 68.35.Rh

I. INTRODUCTION

Compositional and structural changes due to defect formation or phase transitions influence the physical and chemical properties of solids substantially. Oxides are important materials in this respect. The capacity of some oxides to vary their oxygen concentration over a wide range has significance for many technological applications. The oxygen storage capacity of ceria for instance is exploited in automobile catalytic converters to adjust the oxygen concentration by removing or adding oxygen to the exhaust-gas during lean or rich cycles, respectively.[1–3]

At surfaces, atoms are less coordinated, which allow compositional changes to occur even more readily than in the bulk of many oxides. Indeed, the consumption of surface lattice oxygen by reactants is believed to be part of the catalytic cycle in oxide-based oxidation catalysts, i.e., the so-called Mars–Van Krevelen mechanism.[4] Compositional changes at surfaces would also imply significant variations in physical and chemical properties, and thus provide a mechanism by which these properties can be tuned. Recent advances in density functional theory now allow the incorporation of the chemical potential of the gas phase to calculate the thermodynamic stability of different surface structures and composition as a function of changes in the environment.[5] This provides a means to obtain insight with respect to how surface chemistry may change as one moves from the ultrahigh vacuum (UHV) conditions of traditional surface science to more realistic conditions encountered in applications. These studies find that some oxide surfaces are oxygen deficient compared to the bulk stoichiometry under reducing conditions and yet other surfaces can accommodate excess oxygen at high oxygen chemical potential of the gas phase. Furthermore, these compositional changes do not necessarily require a restructuring of the surface but can be accomplished by occupying or vacating surface sites. The variability of the surface oxygen concentration may have important implications for understanding the properties of

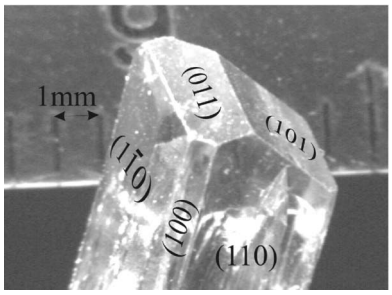

FIG. 1. Photograph of SnO_2 crystal grown by vapor phase transport (Ref. 17). Natural growth faces are {110}, {100} (equivalent to {010} in rutile), as well as {101} (equivalent to {011} in rutile) surfaces.

these materials in technological applications. For example, the occupation of additional sites (cus sites) by oxygen on the RuO_2(110) surface has been linked with the high efficiency of RuO_2 as a CO oxidation catalyst.[6]

In the study presented here the surface properties of stannic oxide (SnO_2) are investigated. Stannic oxide finds technologically important applications as a solid-state gas sensing material for detection of oxidizing and reducing gases,[7–15] as an oxidation catalyst,[16,17] and a transparent electrode material.[18] A review of the applications and material and surface properties of SnO_2 is given in Ref. 19.

SnO_2 crystallizes in the rutile structure. Naturally occurring growth faces of SnO_2 are the {110}, {101} (equivalent to {011}) faces, as well as the {100} (equivalent to {010}) faces. An example of a SnO_2 crystal grown by vapor transport[20] that exposes these low index faces is shown in Fig. 1. This particular crystal and similar specimens have been used in the studies reported here. It appears reasonable to assume that the same crystal faces like the one for macroscopic crystals are also exposed in micro- and nanocrystalline films. It is not known how different surfaces contribute to the gas response of polycrystalline sensor materials or how they differ in their catalytic properties. Conductivity measurements on whiskers with predominantly {010} and {101} planes,[14] nanobelts with {101} surfaces,[15] and sheet conductance measurements on (110) surfaces[13] indicate that all SnO_2 surfaces possess gas sensing properties. The goal of this work is to obtain a more detailed atomistic understanding and characterization of the similarities and differences between these surfaces.

The vast majority of previous surface science studies of single crystal SnO_2 were performed on the (110) surface. This is the most common surface, but as Fig. 1 shows other low index faces are always exposed as well. Calculations showed that the {110} surface has the lowest surface energy, followed by the {100} surface; and then the {101} surface.[21–23] These calculations were performed for bulk truncated, stoichiometric surfaces, however. In this paper it is shown that different (reduced) surface compositions may become thermodynamically favored for low oxygen chemical potentials. In agreement with the results discussed here, Bergermayer and Tanaka[24] have recently performed *ab initio* thermodynamics calculations for the SnO_2 (110) and (101) surfaces and showed that under reducing conditions the (101) surface actually posses a lower surface energy than the (110) surface. It should be mentioned, though, that the structure of the reduced (110) surface is still somewhat in dispute.

Experimental surface science studies under ultrahigh vacuum (UHV) conditions of the (110) surface are summarized in Ref. 25 and references therein. Briefly, this surface shows a series of reconstructions if prepared by sputtering and annealing cycles. The most dominant reconstruction is a 4×1 structure. In order to prepare a stoichiometric 1×1 surface the surface has to be exposed to high pressures of O_2,[26,27] N_2O,[28,29] or oxygen plasma[30] at an elevated temperature of about 700 K. Low-energy He^+ ion scattering spectroscopy (LEIS) showed that the [O]/[Sn] ratio increases sharply after high pressure oxygen treatment.[26] Our previous studies[25] showed that exposing the (110) surface to just 10^{-3} mbar O_2 at 800 K sufficed to obtain a 1×1 LEED pattern. STM studies of this surface however showed a high density of defects. Cox *et al.*[26] used ultraviolet photoemission spectroscopy (UPS) to judge the composition of the SnO_2 (110) surface after oxygen treatment. From their studies they concluded that the samples needed to be exposed to an oxygen pressure of at least 1 Torr to obtain a stoichiometric surface. This conclusion was based on the disappearance of defect states within the band gap of SnO_2.

Electronic structure calculations of the bulk valence band (VB) of SnO_2 find that the top of the VB is mainly O $2p$ derived. In the intermediate region the O $2p$ orbitals mix and form bands with the Sn $5p$. At the bottom of the VB the O $2p$ orbitals overlap strongly with the Sn $5s$.[31,32] The bottom of the conduction band (CB) of SnO_2 is primarily Sn $5s$ and the top Sn $5p$, with a small amount of O $2p$ character mixed in across the entire CB.[31] For SnO the Sn $5s$ states that form the bottom of the CB for SnO_2, become occupied and form the top of the VB.[33,34] In photoemission spectra of SnO these Sn $5s$ derived states show up as a peak at a binding energy of around 2 eV below the Fermi edge.[34] The remainder of the valence band exhibits a resemblance to the SnO_2 VB structure. Thus there are four distinct features in the VB-spectrum for SnO and the total width of the VB for SnO is $\sim$2 eV wider than that for SnO_2.

For *stoichiometric* bulk truncated surfaces, a surface state within the bulk band gap of SnO_2 was predicted in most calculations.[35–37] Because it has been recognized that the (110) surface reduces easily, theoretical investigations focused on the impact of oxygen vacancies and surface reduction on the electronic structure. A popular choice for a model of a reduced surface in theoretical calculations has been a surface with all the bridging oxygen atoms removed from the stoichiometric bulk termination.[36–39] Although such a surface termination had been proposed from the observation of 1×1 LEED patterns and surface reduction derived from He^+ ion scattering experiments,[26] there exists no direct experimental evidence that such a surface structure can be prepared. Nevertheless, the calculations for this hypothetical surface show a strongly dispersed band gap state that is separated by 2 eV from the bulk VB maximum at the M point of the surface Brillouin zone. This band gap state arises from the fourfold-coordinated Sn atoms and is mainly of Sn s- and p-type character.[36,37] Other oxygen defect structures have also been considered.[35,40] For all structures with removed oxygen atoms, defect states within the bulk band gap were

calculated. For fourfold and even more so for threefold coordinated surface Sn atoms, similarities with tin monoxide have been proposed. Some of the charge of broken Sn-O bonds was localized along the direction of the broken bond in the form of Sn lone electron pairs. Such a charge distribution gave rise to states close to the Fermi level.[40] In our calculations we have identified a 1×1 structure for the (110) reduced surface that is lower in energy than others previously considered. The electronic structure of this surface, discussed in detail below, also has less strongly dispersing surface states within the bulk band gap in better agreement with experiments.

Photoemission studies of *reduced* SnO_2(110) surfaces consistently showed the existence of band gap states.[32,26,41–43] Resonant photoemission studies on a band gap state at 1.4 eV above the bulk VB maximum, created by ion sputtering of a (110) surface, indicated that this state was likely to be of Sn 5*s* in origin.[32]

The largest uncertainty in experimental studies arises from difficulties in preparing well-defined SnO_2(110) surfaces. STM studies have shown that the 4×1 reconstruction can be prepared uniformly across the surface. However, the structure and composition of this reconstruction is still a matter of dispute.[25] Here we demonstrate that other low-index SnO_2 surfaces do not suffer from the same uncertainties as the (110) surface. The (101) and the (100) surfaces can be prepared with 1×1 bulk truncations that exhibit SnO or SnO_2 stoichiometries. However, no previous experimental or theoretical studies of the electronic structure have been reported for these surfaces. Here we report a comprehensive study of the structure, composition, and electronic properties of the reduced and stoichiometric (110), (100) and (101) SnO_2 surfaces.

II. EXPERIMENTAL AND THEORETICAL TECHNIQUES

A. Experimental

Structural and compositional characterization was performed in a UHV chamber equipped with instruments for scanning tunneling microscopy (STM), low energy electron diffraction (LEED), and low energy He^+-ion scattering spectroscopy (LEIS). STM images were obtained under empty-state imaging conditions with a positive sample bias voltage in the range of 1–2 V. LEIS was performed with 1200 eV He^+-ions and a scattering angle of 137°. The ion current on the sample was ~15 nA. For temperature programmed LEIS a 0.2 K/s temperature ramp was applied to the sample and a spectrum was obtained every ~10 K.

SnO_2 single crystal samples were mounted with Pt wires spot welded to corrosion resistant Hastelloy™ plates. These materials were chosen to avoid oxidation of the sample mounting during high pressure oxygen treatment. In all studies the natural growth faces of the crystals (see Fig. 1) were investigated without any further polishing. Samples were cleaned by standard sputtering (1 keV Ar^+) and annealing cycles. The cleanliness of the sample surface was checked by LEIS. UHV prepared samples were characterized by LEED and STM. Subsequently, the samples were exposed to 1–100 mbar O_2 in a modified loadlock system of the UHV chamber. The high oxygen pressure was measured with a UHV-compatible thermocouple gauge. This "high-pressure cell" contained a homemade button heater that allowed heating of the sample to ~600 K at elevated oxygen pressures. The button heater consisted of a resistively heated $Pt_{87}Rh_{13}$ alloy wire, 0.1 mm in diameter, that was attached with ceramic adhesive[44] to the backside of a 0.5 mm thick, 10 mm diameter sapphire disk. Tungsten leave springs pressed the Hastelloy™ sample plate against the front of the sapphire disk of the button heater.

The SnO_2 surfaces were oxidized by exposure to 10 mbar O_2 for ~10 minutes at 300 °C, followed by annealing in vacuum to ~500–600 °C, and a second oxidation cycle in the high-pressure cell. Two oxidation cycles were employed to reduce oxygen deficiencies in the bulk, induced by preferential oxygen sputtering during UHV cleaning procedures. To avoid thermal desorption of oxygen from the surface, the samples were cooled down in an oxygen background pressure below ~100 °C before the high-pressure cell was evacuated and the samples were transferred to the UHV chamber.

Angle resolved photoemission spectroscopy (PES) experiments were performed at the 3 m TGM synchrotron beamline[45] at the Center for Advanced Microstructures and Devices (CAMD) in Baton Rouge, Louisiana. The end station was equipped with an ion gun and *e*-beam heater for sample preparation, a front view LEED screen and a rotatable electrostatic analyzer allowing measurements over a wide range of emission angles. The binding energies of all photoemission spectra are referenced to the Fermi edge measured on the molybdenum sample holder.

In the synchrotron end station the samples were cleaned by 1 keV Ne^+ ion sputtering and subsequent vacuum annealing. In order to reoxidize the surfaces after cleaning in UHV, the samples were transferred to an attached load lock and exposed to high pressure (10–100 mbar) O_2. The samples were heated to 300–400 °C during the oxidation process and cooled down in an oxygen atmosphere. Annealing of the sample under high oxygen pressure was accomplished by radiative heating from a resistively heated Pt/Rh wire brought into close proximity of the backside of the sample mounting plate. If not otherwise stated the spectra were acquired with incident light at 45° with respect to the surface normal (*s* and *p* polarized light) and the photoelectrons were collected at normal emission.

B. Theoretical

Total energy calculations and full relaxations were performed using all electron first principles density-functional theory, the PBE[46] generalized gradient approximation to the exchange-correlation functional and atom-centered, polarized, split-valence numerical basis sets (DNP) as implemented in the DMol^3 program.[47,48] Optimized bulk lattice constants were 4.8363 Å and 3.2742 Å, compared to 4.7373 Å and 3.1864 Å for the experimental values. Spin-restricted calculations were run on periodic slabs containing fifteen atomic layers for the O-terminated surface and thirteen atomic layers for the Sn-terminated surface with 10 Å

vacuum separation in the supercells. No symmetry constraints were imposed, and all atoms in the slab were allowed to relax. The slabs were of sufficient thickness that the central layers exhibited the bulk structure. A uniform *k*-point mesh with 18 points was used for the entire surface Brillouin zone. Mulliken population analysis, although not an absolute measure of the exact charge distribution, does yield a consistent measure of relative charge and was used to determine relative oxidation states of atomic species. For Sn(IV) in the bulk SnO_2, the Mulliken population was typically 1.95 to 2.0 *e*. This did not vary by more than ±0.05 for Sn(IV) atoms on the stoichiometric or partially reduced surfaces for all three low index surfaces investigated. For atoms on reduced surfaces whose coordination were consistent with Sn(II) oxidation, the Mulliken population was consistently 0.97 to 1.05 *e*. These results were crosschecked by Hirshfeld population analysis, which uses a slightly different partitioning scheme. The relative Hirshfeld values were very consistent, ranging from 0.71 to 0.73 *e* for Sn(IV) in the bulk and on the surface, and 0.41 to 0.43 *e* for Sn(II) on the reduced surfaces. In all cases for both population analysis techniques, the surface tin atoms with a formal +2 oxidation state had approximately half the positive charge distribution of the bulk and surface atoms with a formal +4 state, and were readily distinguishable.

The 0 K total energy calculations were linked to the finite temperatures and pressures encountered in the experiments through the recently developed method of *ab initio* thermodynamics.[5,6,24,49–54] The change in chemical potential $\Delta\mu_i$ for species *i* as a function of temperature for Sn metal, SnO_2(c), and O_2(g) were taken from thermodynamic reference tables.[55,56] The change in chemical potential for the slabs as a function of temperature was assumed to be comparable to bulk SnO_2. The difference in vibrational entropy between the surface and the bulk phonons for a metal oxide (RuO_2) when no hydrogen is present has been estimated to contribute less than ±10 meV/Å^2 to the surface free energy in absolute terms, and considerably less in relative surface free energies.[6]

Band structure and density of states (DOS) calculations were performed on the most relevant, i.e., lowest surface free energy, structures. Scalar relativistic corrections were added using methods described in Ref. 57, the slabs were widely separated on the order of 100 lattice constants. Stoichiometric slabs contained 66 atoms in the primitive slab cell. *k*-point sampling was done on a 6×6 unshifted mesh and checked with a 12×12 mesh. In the band structure figures the surface states are superimposed on the bulk states projected onto the surface. The Mulliken population of the surface atom is represented by the dot size of the surface bands in the band structure diagrams. A scissor operator was used to adjust the calculated band gap to the experimental value of 3.6 eV.

III. RESULTS

The composition, structure, and electronic properties of three low index SnO_2 surfaces were studied by LEED, LEIS, STM, and ARUPS. In STM studies, all SnO_2 surfaces exhibited an additional modulation or bumpiness with varying modulation heights of up to 0.1 nm and widths of tens of nanometers. This has been reported previously for the (110) surface,[25] where we also observed spatial variation in the electronic structure associated with the bumps. Subsurface structural defects, such as dislocations, and/or variations in the local oxygen concentration were proposed to explain the sub-nanometer-height surface modulations. The observation that this corrugation exists on all three low index surfaces studied here supports the existence of such subsurface defects. Hence these features will not be discussed further in the interpretation of the STM images.

The extreme surface sensitivity of He^+ scattering allows identification of atomic species in the topmost surface layer. A quantitative determination of the surface composition is not possible in most cases, however, because of unknown scattering cross-sections and neutralization probabilities for the He^+ ions interacting with different target atoms and atomic shadowing effects. These limitations also make obtaining absolute numbers problematic for the surface composition in the case for He^+ scattering from the various SnO_2 surfaces. A variation of the oxygen and tin peak intensities for identical scattering conditions is significant, however, and does indicate changes at the sample surface. Intensity changes in ion scattering may have different origins. Surface morphologies (roughness) as well as changes in the neutralization probabilities of He^+ ions at the surface due to, for example (temperature dependent) electronic changes may affect the measured intensities.[58–60] Despite of all these uncertainties, He^+-LEIS is an effective tool for measuring relative compositional changes at surfaces. *A decrease in the oxygen signal concurrent with an increase in the tin signal is an unambiguous sign for oxygen depletion from the surface layer*. Continuous monitoring of the surface composition with LEIS while the sample temperature is ramped allows determination of critical temperatures at which compositional changes occur at the surface. Preferential sputtering of one surface species by the probing He^+ ion beam could also induce a compositional change in the course of the experiment. For such an effect a continuous change in composition with time would be expected. In addition we excluded the possibility for a strong impact due to preferential sputtering by comparing the LEIS peak ratios directly after oxidation and high temperature annealing. In the following the findings for the three low index surfaces are presented separately.

A. SnO_2(100) surface

1. SnO_2(110)*: Composition and structure—experiment*

The structure of the (110) surface after UHV preparation has been studied extensively. Our STM and LEED studies confirm the previous observations and are summarized in Ref. 25 and the brief review given above. For completeness we mention that a (4×1) reconstruction forms after standard sample preparation, i.e., ion sputtering and vacuum annealing to ~980 K. It is important to note that exposure to high oxygen pressure at room temperature, at least up to a pressure of 200 mbar, does not lift the (4×1) reconstruction. Annealing of the sample to 500–600 K in an oxygen atmo-

sphere is needed to remove the 4×1 reconstruction and to form a surface that exhibits a 1×1 LEED pattern with a significantly increased O/Sn ratio in LEIS studies. It was reported that a 4×1 reconstruction reforms if an oxidized sample is heated under vacuum to ~900–1000 K. Interestingly, we find that the structure one obtains after annealing of an oxidized surface in vacuum depends on the oxidation "history" of the sample. Samples that were extensively cleaned under UHV conditions, i.e., many cycles of sputtering and annealing, revert to a 4×1 structure upon UHV annealing to ~900–1000 K of an oxidized sample, in agreement with previous reports. However, if the sample is oxidized and vacuum annealed at least twice, without any further sputtering of the sample, then the 4×1 reconstruction is not recovered. Instead, a 1×1 LEED pattern is observed up to ~1000 K followed by the formation of a 1×2 superstructure for higher annealing temperatures. This implies that reduction by vacuum annealing of a fully oxidized, stoichiometric SnO_2 sample does not form a 4×1 reconstruction but directly converts from a 1×1 structure to a 1×2 superstructure. Consequently, the 4×1 reconstruction appears to be an "artificial" structure that forms only because of the sample preparation conditions employed, i.e., ion sputtering and vacuum annealing, which results in an oxygen deficient near-surface region.

Cox *et al.* were the first to evaluate the composition of $SnO_2(110)$ surfaces by LEIS.[26] Here similar studies were performed and the evolution of the oxygen and tin scattering peaks with sample temperature in LEIS are shown in Fig. 2(a) for the (110) surface. The measurements discussed here were performed on thoroughly oxidized samples, i.e., samples that did not convert to a 4×1 reconstruction after high temperature vacuum annealing. Initially, at low temperatures, the oxygen signal is stronger than the Sn scattering peak. At higher temperature this is inverted. A transition occurs in a temperature range of 440–520 K. This transition is somewhat more clearly defined for the oxygen scattering peak, which stays roughly constant up to ~440 K then up to 520 K the peak intensity sharply drops. For even higher temperatures the oxygen peak continues to decrease (and the tin peak increases), but at a much smaller rate. The continuous change in the Sn/O ratio indicates further loss of oxygen from the surface at higher temperature. In qualitative LEED studies no transition is discerned at this temperature and only a 1×1 pattern is observed. To further characterize the surface structure STM was employed.

STM studies on an oxidized surface are considerably more difficult than studies on $SnO_2(110)$ surfaces prepared in vacuum. The main reason is that the samples roughen significantly during the oxidation process and only terraces of nanometer widths are observed. No atomic-scale resolution was obtained on these narrow terraces. A typical STM image for such a surface is shown in Fig. 3(a). Although the terraces are narrow a clear preferential alignment of the step edges along the [001], and to a lesser extent, along to the [110] direction is observed. Bright features of 1–2 nm in height are frequently observed on these surfaces. The origin of these features is not clear, but some kind of contamination cannot be excluded. Upon annealing of the oxidized samples in UHV to ~900 K, slightly larger terraces form but the

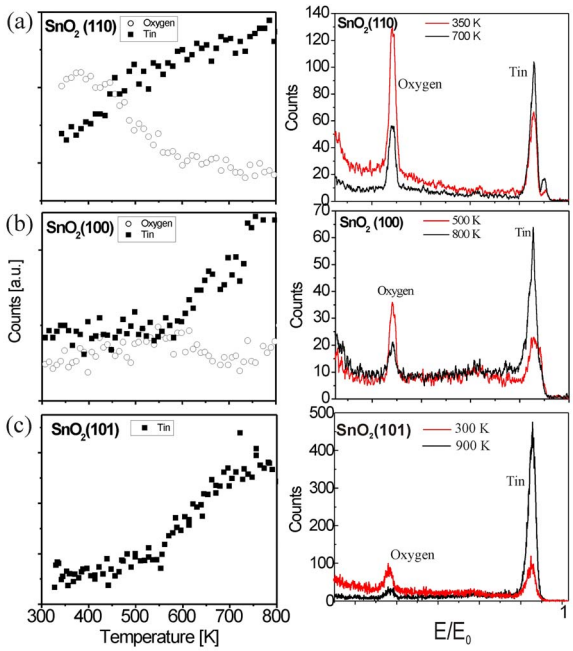

FIG. 2. (Color online) Temperature programmed low energy He^+ ion scattering (LEIS) studies of the SnO_2 (a) (110), (b) (100), and (c) (101) surfaces. The samples were fully oxidized by a high pressure O_2 treatment prior to ramping up the temperature in UHV. The oxygen and tin signals were monitored and are plotted with respect to sample temperature. Concurrent decrease of the oxygen signal and increase of the tin signal indicate the formation of a reduced surface phase. Phase transitions are observed at 440–520 K for the (110) surface, 610–660 K for the (100) surface, and 600–700 K for the (101) surface. In the right panel the LEIS spectra for E_p=1220 eV are shown before and after annealing to temperatures above the phase transition.

surface is still quite rough [Fig. 3(b)]. Additionally the terraces do not appear atomically flat anymore but exhibit some corrugation. This disordered appearance of the surface raises the question of whether the observed 1×1 LEED pattern truly reflects the periodicity of the surface, or if the surface has no long range order with the observed LEED pattern originating from the subsurface region. At annealing temperatures of 1000 K, a diffuse 1×2 LEED pattern appears. In STM larger terraces of tens of nanometers in width are imaged [Fig. 3(c)]. Figure 3(d) shows rows running along the [001] direction with a periodicity in the [110] direction of twice the lattice constant of SnO_2. This periodic feature is responsible for the diffuse 1×2 diffraction pattern. On the close-to-atomic scale, however, these rows do not appear well ordered and regions remain at the surface that exhibit complete disorder. The corrugation of the rows is in the range of 0.15–0.3 nm, which is of the order of atomic step heights. The large variation in the corrugation reflects the high density of irregularities in this structure.

A 1×2 superstructure has also been observed for $SnO_2(110)$ surfaces prepared by vacuum preparation only. Such a 1×2 structure forms at high annealing temperatures of ~1200 K subsequent to the formation of the 4×1 reconstruction.[61] Similarities in STM images of the 1×2 high-temperature phase for vacuum prepared samples[61] and

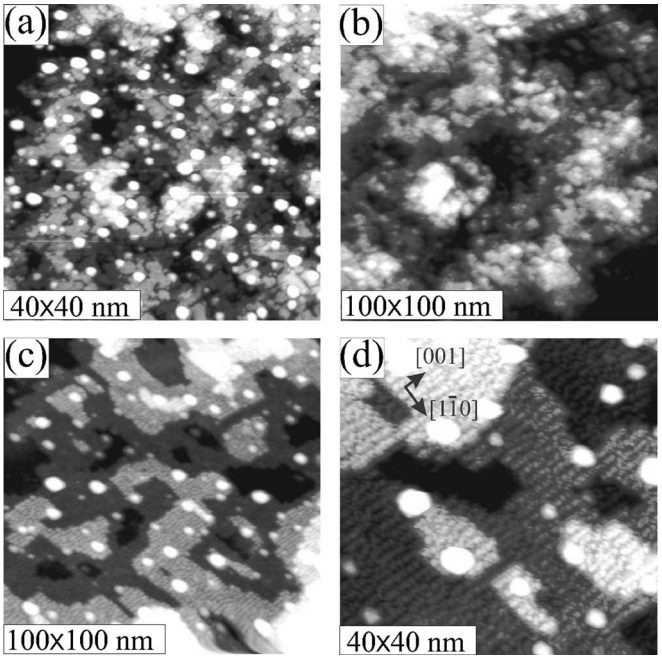

FIG. 3. STM images of the (110) surface. (a) Surface after high pressure oxidation; scan area 40 nm$\times$40 nm. (b) Surface after annealing in UHV to 900 K; scan area 100 nm$\times$100 nm. (c) and (d) Surface after annealing to 1000 K, a 1×2 reconstruction is formed; scan area 100 nm$\times$100 nm (c), and 40 nm$\times$40 nm (d).

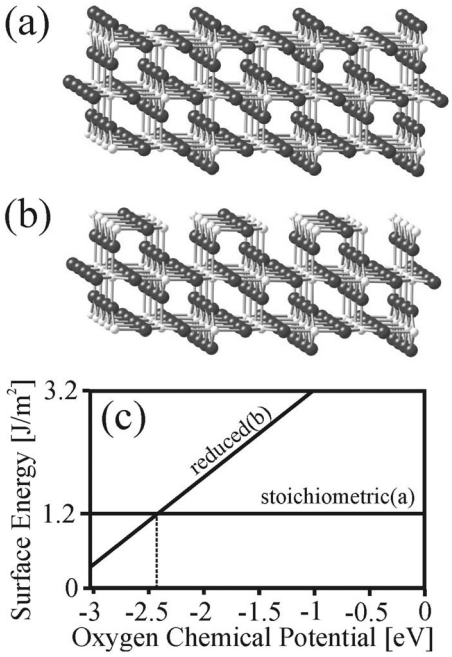

FIG. 4. Ball-and-stick models for (110) surface structures for (a) stoichiometric surface and (b) reduced surface. The dependence of the surface energy of these two models on the oxygen chemical potential is plotted in (c).

the 1×2 structures obtained by annealing a fully oxidized sample in vacuum suggest that these are identical surface structures. Such a conclusion implies that the "artificial" 4×1 structure on the sputtered and annealed surfaces hinders the formation of the 1×2 phase at lower annealing temperatures.

LEIS and STM indicate that preparation of a fully oxidized surface with large flat terraces is challenging for the (110) surface. After high-pressure oxidation only small terraces are observed. This roughening may be a result of Sn interstitials diffusing to the surface where they interact with oxygen to grow SnO_2 adlayers, similar to oxidation mechanisms observed on $TiO_2(110)$.[62,63] In order to obtain large, flat terraces high temperature annealing is needed. However, LEIS indicates that oxygen is lost from the surface even after mild annealing in UHV and although larger terraces form, these terraces exhibit a roughness that indicates a very high defect concentration consistent with formation of a nonstoichiometric surface layer. The alternative to vacuum annealing is annealing in an oxygen atmosphere. Attempts at prolonged oxygen annealing resulted in a sample with a high resistance, however, causing charging of the sample during LEED and making STM measurements impossible.

2. $SnO_2(110)$: *Composition and structure—DFT calculations*

Ab initio thermodynamics calculations of the free energy of the stoichiometric 1×1 surface observed after annealing in oxygen are consistent with the overwhelming stability of this surface at the upper limit of the oxygen chemical potential. The surface energy and structures shown schematically in Fig. 4 is in agreement with the calculated results for the stoichiometric surface of Bergermayer and Tanaka.[24]

When this fully oxidized stoichiometric surface is annealed at about 500 K, the sample loses surface oxygen but retains a 1×1 LEED pattern up to $\sim$900 K. The lower oxygen signal in LEIS and the 1×1 LEED pattern led to the speculation in earlier work[26] that the twofold bridging oxygen atoms are removed from the surface. Oviedo and Gillan did a very thorough theoretical investigation of reduced (110) surfaces containing either bridging or in-plane oxygen vacancies.[35] Their DFT results indicated that in general, in-plane vacancies have a lower formation energy for 1×1 structures than bridging oxygen vacancies, particularly at high concentration. The in-plane vacancies also have an attractive interaction such that rows of in-plane vacancies are preferred over isolated or staggered arrangements. They did not examine systems having *both* bridging and in-plane vacancies, however. We have found that the lowest energy 1×1 structure in the UHV limit does contain *both* bridging and in-plane oxygen vacancies to yield the structure in Fig. 4(b). In this structure, all bridging oxygen atoms are removed, plus every other row of in-plane oxygen atoms, i.e., one row per unit cell. The dependence of the surface energies of the stoichiometric and the reduced surfaces on the oxygen chemical potential is shown in Fig. 4(c). From this diagram it can be seen that the surface energy of the reduced surface is lower than the surface energy of the stoichiometric surface for oxygen chemical potentials of the system lower than -2.4 eV. Thus under such extreme reducing conditions the reduced surface is thermodynamically favored over the stoichiometric surface. The reduced surface structure leaves threefold coordinated tin and oxygen atoms at the surface and a surface layer with SnO composition. Thus Sn is attain-

ing a 2+ oxidation state. Furthermore, such a surface structure still exhibits a 1×1 unit cell.

Annealing the reduced 1×1 surface at 900 K, however, showed significant disorder in the STM image. In order to determine what surface features might contribute to the disorder under high vacuum conditions, over 25 different surface structures were evaluated. These structures included previously proposed structures for 4×1 reconstruction with periodically removed in-plane oxygen atoms,[64] various different arrangement of removed surface oxygen atoms, as well as constellations of threefold coordinated Sn atoms in nonbulk positions. In addition to the lowest energy structure shown in Fig. 4(b), several other structures very close in energy were found which may be responsible for the disorder observed in STM images. One group of structures was found which resulted from the facile removal of additional in-plane oxygen atoms from the fully occupied rows in between the rows of oxygen vacancies. Removal of every other in-plane oxygen from this row creates a $c(2\times2)$ structure with a surface energy of 0.42 J/m^2 at the UHV limit (lowest oxygen chemical potential). Removal of every other *pair* of in-plane oxygen atoms is slightly more favorable, producing a (4×1) structure with a UHV limit surface energy of 0.41 J/m^2. Although this structure, with one complete row of in-plane oxygen atoms removed and every other pair removed in alternate rows, is lower in energy than other 4×1 structures proposed previously, including one in which *every* row has pairs of in-plane oxygen atoms removed (0.63 J/m^2), it does not describe the experimentally observed 4×1 structure because it does not possess the observed glide plane symmetry.[65] Removal of all in-plane oxygen atoms yields a 1×1 structure that is also comparable in energy, at 0.45 J/m^2. This leaves a row of tin atoms that are almost neutral, coordinated to a single oxygen atom below. These almost neutral tin atoms can be viewed as the starting point for formation of metallic Sn. Metallic Sn has a high vapor pressure and thus would likely desorb from the surface at high annealing temperatures used for sample preparation. The presence of many structures with similar energies indicates that there are not sufficiently strong energetic preferences to induce long-range order in the removal of the in-plane oxygen atoms to form the structure shown in Fig. 4(b) only and this may explain the somewhat disordered surfaces seen in STM images obtained on samples prepared at 900 K. It also should be noted that the relative stability of these extremely reduced surfaces is very sensitive to the oxygen partial pressure due to the high deviation from stoichiometry.

For annealing temperatures above ~1000 K a 1×2 reconstruction forms. STM images show that this structure is extremely defective and no atomic scale features could be deduced from these images that would aid in deriving a model for this surface phase. It has been speculated previously that this structure is isostructural to the 1×2 reconstruction observed on the rutile-TiO_2(110) surface.[61] Two models have been previously proposed for the 1×2 reconstruction: one model suggested by Onishi *et al.* with a Ti_2O_3 composition,[66] and a second consisting of missing bulk units and removed bridging oxygen atoms.[67] Calculation of the SnO_2(110)-1×2 model isostructural to the Ti_2O_3 model, showed that the surface energy of this structure at 1.36 J/m^2 is higher than the 1.21 J/m^2 stoichiometric surface even under UHV conditions, and becomes less stable as the oxygen chemical potential increases. Therefore, it is highly unlikely that this structure, with an improbable oxidation state of +3 for Sn, would ever form. The second structure with missing bulk units and removed bridging oxygens is also higher in energy. We have identified a third model with a 1×2 structure that is thermodynamically stable over a narrow range (<0.2 eV) of oxygen chemical potential, as shown in Fig. 4(c). In this structure every other row of bridging oxygen atoms is removed from the stoichiometric surface. If the oxygen chemical potential is slightly higher, these bridging oxygen vacancies will be filled at equilibrium to restore the stoichiometric surface. If the oxygen chemical potential is reduced, then all the bridging oxygens will be removed as well as a row of inplane oxygen atoms to generate the lowest energy (1×1) reduced surface shown in Fig. 4(b). It is important to note, however, that this structure with a 1×2 periodicity cannot be the structure observed in STM images. This is mainly because of the large corrugation observed for the 1×2 structure both in STM and atomic force microscopy (AFM).[61] Thus at the moment no satisfactory model for the (110)-1×2 structure exists.

3. SnO_2(110): *Electronic structure*

The (110) surface is the only one of the three surfaces investigated here that has been studied before by photoemission spectroscopy. Previous studies on the (110) surface were, however, limited to samples prepared under UHV conditions and specifically focused on the 4×1 reconstruction and defective surfaces prepared by sputtering.[32,42] The next subsection shows that the surface electronic structure of the (110) surface depends critically on preparation conditions and the consequent state of oxidation, followed by a discussion of resonant photoemission studies. We close the report for the (110) surface by presenting the results from electronic structure calculations for a hypothetical surface with only the bridging oxygen atoms removed, a reduced $Sn^{2+}O^{2-}$ surface, and the bulk-terminated, stoichiometric SnO_2(110) surface.

(1) Preparation dependent photoemission. Figure 5 shows VB spectra of SnO_2(110) surfaces prepared in several ways. It is apparent that one can obtain very different results depending upon the sample treatment. In Fig. 5(a) the sample was prepared by standard vacuum preparation, i.e., several cycles of sputtering and annealing to ~700 °C. Consequently the sample exhibited a 4×1 LEED pattern. In Fig. 5(b) the sample was exposed to ~20 mbar O_2 at a sample temperature around 300 °C. This sample exhibited a 1×1 LEED pattern. Subsequent annealing in UHV to 600–700 °C resulted in the reformation of a 4×1 LEED pattern and the corresponding PES is shown in Fig. 5(c). Oxidation at oxygen pressures of 100 mbar and at 300 °C sample temperature caused a disordering of the surface that resulted in the disappearance of any LEED pattern. This disordering is also apparent from the broad, poorly defined valence band spectra shown in Fig. 5(d).

The most obvious changes in the valence band spectra of these surfaces are observed in the band gap region. Only

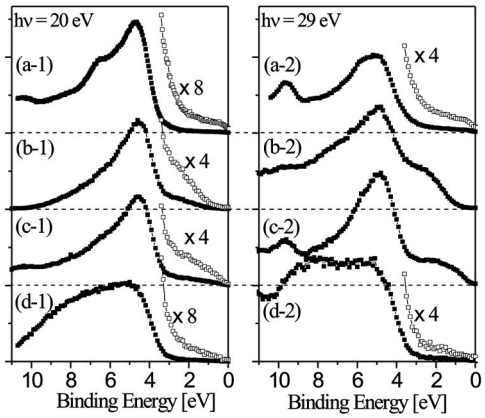

FIG. 5. Photoemission spectra for differently prepared $SnO_2(110)$ surfaces acquired with photon energies of 20 eV (left panel) and 29 eV (right panel). (a) Surface prepared by cycles of sputtering and vacuum annealing to ~700 °C. This surface exhibits a 4×1 LEED pattern. (b) Surface oxidized in ~20 mbar O_2. A 1×1 LEED pattern is observed. (c) Surface in (b) annealed to ~700 °C in vacuum. This annealing procedure reformed a 4×1 LEED pattern. (d) Surface oxidized at above 100 mbar O_2 pressure.

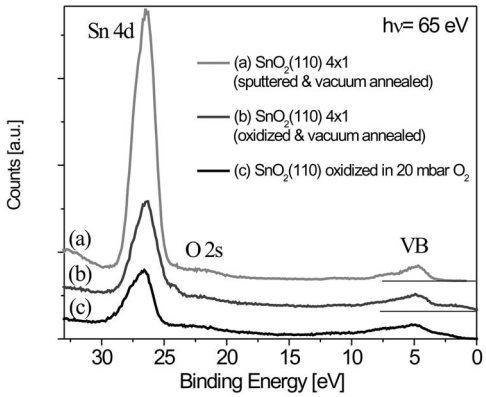

FIG. 6. Wide scan photoemission spectra acquired with a photon energy of 65 eV for three differently prepared samples: (a) 4×1 reconstructed surface, prepared by sputtering and annealing. (b) 4×1 reconstructed surface, prepared by vacuum annealing of an oxidized surface. (c) 1×1 surface prepared by oxidizing in 20 mbar O_2. The spectra are offset for clarity and normalized to the valence band maximum.

surfaces prepared at high oxygen pressures [Fig. 5(d)] exhibit a bulklike band gap with only residual photoemission from within the gap itself. This residual photoemission intensity may result from surface defects or disorder. The observation that a bulk-band-gap-like surface forms only after exposure to high oxygen pressures is in agreement with UPS studies by Cox *et al.*[26]

Surfaces oxidized under milder conditions at somewhat lower oxygen pressures exhibit photoemission from the band gap region [Fig. 5(b)]. The maximum emission of the band gap states is around 2.5 eV and extends up to 1 eV below the Fermi edge. One can only speculate what exactly the surface structure is that causes these strong band-gap emissions. It is clear that it is not a stoichiometric surface and the surface structure that is assumed to be the most stable reduced surface consists of missing bridging and in-plane oxygen rows (see Sec. III A 2).[24] Such a surface has a SnO surface composition and as such one could intuitively expect surface states similar to states of bulk tin monoxide, i.e., with a Sn-5*s* derived state around 2 eV below the CBM. Calculations of the electronic structure of the reduced and the stoichiometric surfaces are presented below.

It is intriguing that the photoemission intensity from the band-gap region can be very different for 4×1 reconstructed surfaces. Samples prepared by sputtering and annealing alone [Fig. 5(a)] exhibit weak emission from the band-gap region. This is in agreement with previous studies.[32,42] Some emission is observed, however, with states spanning almost the entire band gap up close to the Fermi edge. (4×1)-reconstructed surfaces obtained by vacuum annealing of an oxidized sample [Fig. 5(c)], on the other hand, show a much stronger emission from the bulk band-gap region, but a small band gap of about 0.5 eV remains.

Differences in the Sn/O ratio for the differently prepared surfaces are apparent from the PES intensity of the Sn 4*d* core level measured with a photon energy of 65 eV. Figure 6 shows PES for the binding energy region from 33 eV to the Fermi edge for the same samples used for obtaining the spectra shown in Figs. 5(a)–5(c). These spectra include the Sn 4*d* and weak O 2*s* core levels,[68] as well as the VB region. The spectra were normalized to the maximum intensity of the mainly O 2*p* derived VB. Strong variations in the intensity of the Sn 4*d* level are observed. The samples sputtered and annealed in vacuum show the strongest Sn 4*d* emission [Fig. 6(a)] consistent with a strong depletion of surface oxygen. 4×1 reconstructed samples prepared by vacuum annealing of an oxidized surface show a much reduced Sn 4*d* emission, indicating that although it shares the same reconstruction as the sputtered and annealed surface it possesses a lower Sn/O ratio. These differences in the Sn/O ratio for differently prepared 4×1 reconstructed surfaces may indicate that the 4×1 structure is not just a reconstruction strictly confined to the surface but may involve underlying layers as well. Such an interpretation can also explain the differences in the gap-state emission between the two samples, if most of the band-gap emission originates from the interface region between the 4×1 structure and the "substrate." Finally, the Sn 4*d* emission is smallest for the oxidized sample [Fig. 6(c)]. Additionally a small shift of ~0.25 eV for the Sn 4*d* peak to higher binding energy is observed. This may be explained by a small chemical shift in the 4*d* core levels as is expected for Sn in a 4+ oxidation state compared to a 2+ oxidation state.[33]

(2) Resonant photoemission. VB spectra for photon energies in a range from 20 eV to 35 eV were acquired for 4×1 reconstructed samples prepared by repeated cycles of sputtering and annealing [Fig. 5(a)], and for samples prepared by annealing in 20 mbar O_2 [Fig. 5(b)]. The aim of this study was to use resonant photoemission to verify that the band-gap states of these surfaces contain a significant Sn component. A resonance in the photoemission may be expected if the photon energy is swept through the dipole allowed Sn $4d \Rightarrow$ Sn $5p$ transition threshold. A direct recombination process of the excited Sn atoms with a simultaneous ejection of a valence band electron gives rise to the increased

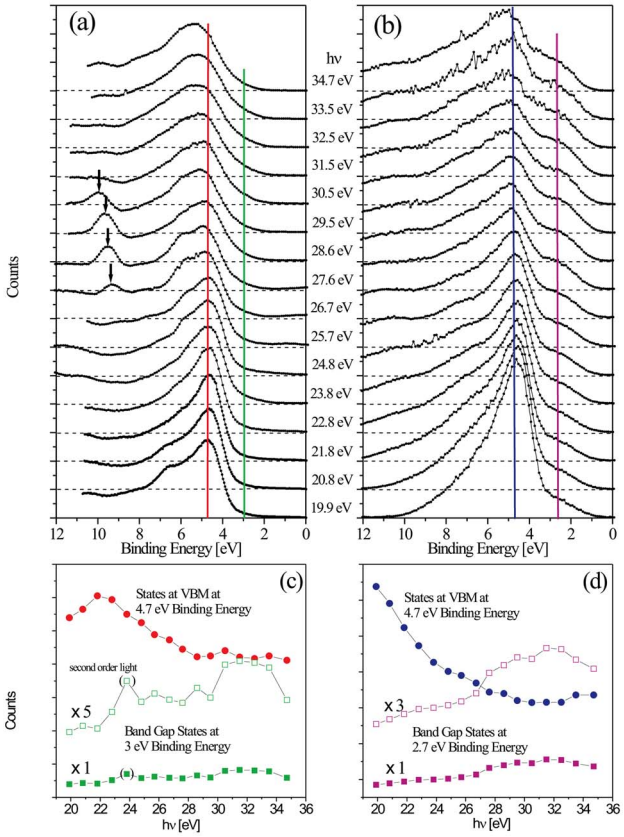

FIG. 7. (Color online) Photoenergy dependence of valence band spectra for an energy range between 20 eV and 35 eV for (110) surfaces. The spectra are normalized to the valence band area. In (a) valence band spectra for a 4×1 reconstructed surface, obtained by sputtering and annealing, are shown. In (b) the valence band spectra of a sample prepared by oxidation in 20 mbar O_2 are displayed. (c) and (d) show the photoemission intensity as a function of photon energy for the binding energies indicated by the lines in (a) and (b), respectively.

emission for photon energies close to the excitation threshold value. A similar resonance was reported previously for an ion-sputtered $SnO_2(110)$ surface.[32] If we assume that the processes involved in this resonance are strictly intra-atomic then it can be concluded that the VB states involved in such a resonance are Sn-derived.

Figures 7(a) and 7(b) shows VB spectra normalized to the VB area for different photon energies for the two differently prepared (110) samples. The photoemission intensity is plotted against photon energies for binding energies of 4.7 eV and 3 eV for the 4×1 reconstructed surface in Fig. 7(c), and for binding energies of 4.7 eV and 2.7 eV in Fig. 7(d) for the sample oxidized at 20 mbar O_2. In both cases the photoemission intensity of the band gap states shows an increase for photon energies between 28 eV and 34 eV. Thus we conclude that the band-gap states on the (110) surface are also Sn-derived in agreement with the measurements performed by Themlin *et al.* for the sputtered $SnO_2(110)$ surface.[32] The intensity plots for the VBM, i.e., a binding energy of 4.7 eV, do not show an enhanced emission in the region of a possible resonance. Consequently, the states at this binding energy appear to be mainly O $2p$ derived for the (110) surface, even for strongly reduced surfaces.

One interesting observation is a strong resonance for the 4×1 reconstructed surface for photon energies between 28 eV and 31 eV at a binding energy of ~9.6 eV [indicated by arrows in Fig. 7(a)]. This resonance is only seen if the surface exhibits a 4×1 reconstruction [see also Figs. 5(a) and 5(c)] and has not been observed for the SnO_2 (101) or (100) surfaces (see below). Thus it is a unique signature for the $SnO_2(110)$-4×1 surface. Interestingly, this resonance state seems to disperse slightly with photon energy, thus it cannot be a pure surface state. This supports our assertion that the 4×1 structure is not a strictly two-dimensional surface reconstruction. Sinner-Hettenbach *et al.* observed resonances at similar binding energies, but higher photon energies, i.e., sweeping through the Sn $4p \Rightarrow$ Sn $5s$ transition.[42] These resonances were also only observed for the 4×1 reconstructed surface but not for a sputtered (110) sample.

Finally we also attempted angle-resolved measurements (not shown) to identify a band dispersion of the band gap states. For the sputtered and annealed surface that exhibits a 4×1 reconstruction, there was no clear peak in the band gap so dispersion could not be measured. For the sample oxidized at 20 mbar, a strong band gap state was detected but no dispersion was observed in angle-resolved measurements. This is likely due to some degree of disorder of the surface. Although we observe a 1×1 LEED pattern, STM measurements on similar samples showed a significant amount of disorder in the surface layer (see Sec. III A 1). Thus the photoemission in the band gap region may be better described by a high density of defects rather than a 2D surface state. Nevertheless, the most common type of "defect" would likely resemble the structure for the reduced (110)-1×1 surface proposed in Sec. III A 2 and in Ref. 24. Two different reduced surface structures as well as the stoichiometric bulk termination have been used for band structure calculations discussed next.

(3) Comparison of experimental results and DFT calculations. Results from band structure calculations for three different bulk terminations are presented in Fig. 8. The stoichiometric $SnO_2(110)$ surface exhibits surface states within the bulk band gap region [Fig. 8(a)], in agreement with previous theoretical studies.[35–37] These two states are nearly flat, with one just above and the other 0.2 to 0.3 eV above the bulk VBM. In the experimental studies mentioned above and in those by Cox *et al.*[26] no surface state for an oxidized (110) surface was observed. It should be noted, however, that the fully oxidized surface prepared in this study was very disordered, as indicated by broad, poorly defined valence band peaks. In addition, the surface band is separated from the VBM by a small amount and hence may be difficult to identify in the experimental studies.

Figure 8(b) shows the band structure calculations for a surface with removed bridging oxygen atoms only. This structure has been included in this study merely for completeness because it has been assumed to be the reduced surface structure of $SnO_2(110)$ in earlier experimental[26] and theoretical studies.[36–39] However, our own calculations (see Sec. III A 2) showed that this structure with only the in-plane oxygen atoms restored and the bridging atoms still missing is

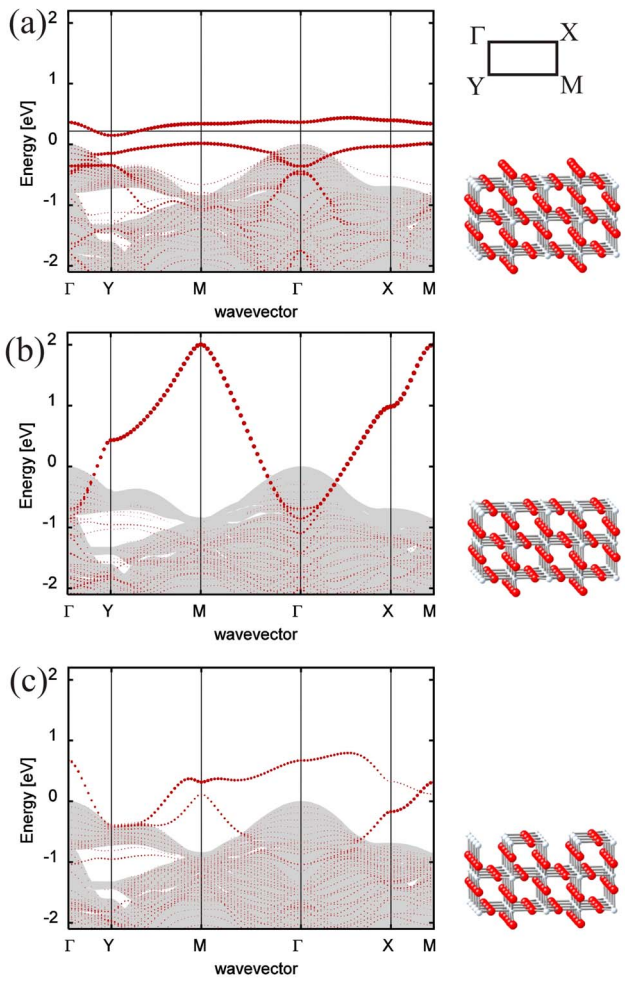

FIG. 8. (Color online) Band structure calculations for SnO_2(110) surfaces with (a) stoichiometric, (b) half-reduced, and (c) reduced bulk terminations. Gray shaded areas represent the projected bulk states; dots represent surface states and resonances. Ball-and-stick models representing the various surface structures are shown on the right. The dimensions of the surface Brillouin zone are the same for all three surface structures and are indicated in the top right corner.

not expected to be accessible, as it is always significantly higher in energy than either the fully reduced structure [Fig. 8(c)] or the stoichiometric surface [Fig. 8(a)]. Furthermore, such a surface would have a strongly dispersed surface state that extends 2 eV above the bulk VBM at the *M* point of the surface Brillouin zone, in agreement with earlier calculations of the same surface structure.[36] In the experimental studies no dispersion of band gap states was observed, clearly indicating that such a surface structure has not been prepared even for surfaces that exhibited a (1×1) LEED pattern.

The electronic structure of the surface with a $Sn^{2+}O^{2-}$ composition that has been identified as the most stable under reducing conditions is shown in Fig. 8(c). This structure also exhibits surface bands in the bulk band-gap region, but they only extend less than 1 eV into the bulk band gap from the VBM. Thus there is some resemblance between the electronic structure calculations for this surface and the PES of the sample prepared at 20 mbar O_2 [Figs. 5(c) and 7(b)]. Consequently, the agreement between the measurements and the electronic structure calculations for this surface gives evidence that this is indeed the dominant surface structure that forms for a reduced SnO_2(110) surface.

For the 4×1 reconstruction, we are of the opinion that a good model does not yet exist. Therefore band structure calculations for surface structures with such a periodicity were not performed.

B. SnO_2(100) surface

1. SnO_2(100)*: Composition and structure*

No previous studies of the (100) surface have been reported. Preparation by sputtering and annealing in a range of 600 K to 1000 K results in a 1×1 LEED pattern. The sample retains its 1×1 LEED pattern even after exposure of the surface to 10 mbar O_2 at room temperature or elevated temperatures ($\sim$600 K). Although no changes in qualitative LEED can be identified, the oxygen to tin peak ratio measured in LEIS increases significantly after high-pressure oxygen exposure. How the oxygen and tin peaks evolve with temperature in LEIS measurements on an initially oxidized surface is shown in Fig. 2(b). From this representation it is apparent that the surface composition changes in a temperature range of 610–660 K. The decrease of the oxygen signal with a concurrent increase in the tin signal indicates a depletion of surface oxygen. Since the dimensions of the unit cell remain unchanged it is proposed that this transition is a consequence of the removal of bridging oxygen atoms from the stoichiometric SnO_2 bulk termination (see the ball-and-stick models in Fig. 9). This leaves threefold coordinated Sn atoms and a surface layer with a SnO composition as indicated in Fig. 9(b). Justification for this assignment also comes from STM measurements and DFT calculations that will be discussed below.

The structure of vacuum prepared surfaces, i.e., with a reduced SnO surface layer, was studied by STM. These studies revealed flat terraces separated by two kinds of steps as can be seen in Fig. 10(a): Type-I steps are straight and are oriented along the [001] crystallographic direction. Type-II steps are less well oriented but are mainly aligned along the [010] direction. The measured step height of step I is close to unit cell height, i.e., 0.48 nm. It can be seen that step II consists of a double step, i.e., two steps with half the unit cell height each. Furthermore, terraces are also traversed by half-unit cell height steps. These steps define elongated "holes" in the terraces with long axes of the holes along the [001] direction. Often these elongated holes terminate at full unit-cell height steps (step I). These elongated holes, and pairs of steps predominantly along the [010] direction, give the surface a "zebra" pattern.

This step morphology can be understood in terms of autocompensated step edges, i.e., step edges that consist of Sn atoms in either of their two preferred valencies. Figure 11 shows a ball-and-stick model for step edges along the [010] and [001] directions of half a unit cell height, the models represent the size of the supercells used in the DFT calculations. Formation of such step edges results in fivefold coor-

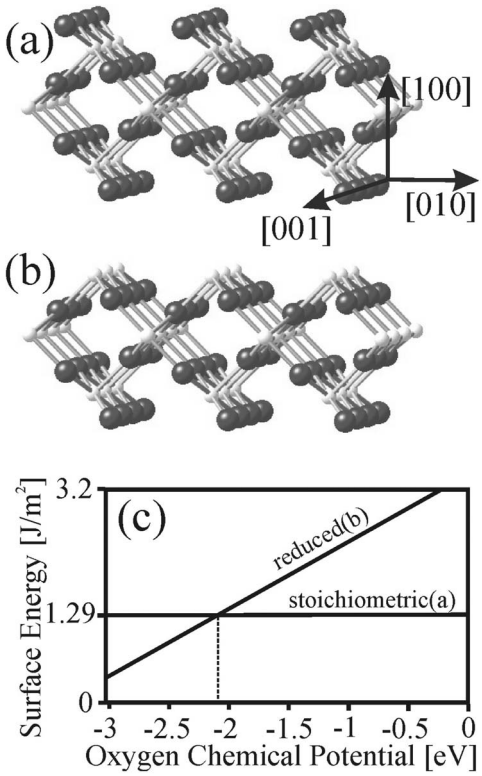

FIG. 9. Ball-and-stick model for two bulk terminations of the (100) surface. (a) Stoichiometric SnO_2 surface and (b) surface with a SnO composition. The dependence of the surface energy of these two models on the oxygen chemical potential is plotted in (c).

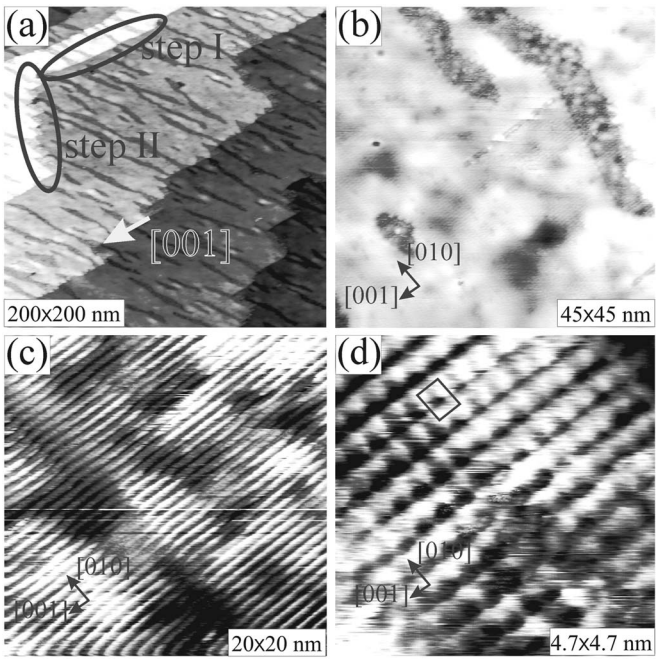

FIG. 10. STM images of the (100) surface after UHV preparation. (a) Large scale scan with a scan area of 200×200 nm. Two kinds of step edges are observed. Unit-cell height steps along the [001] direction (step I) and half-unit cell height steps (step II). (b) Details of "holes" in the terraces surrounded by step II–type step edges; scan area 45 nm $\times$ 45 nm. (c) Atomic rows along the [001] direction; scan area 20 nm $\times$ 20 nm. (d) Atomic resolution image with the 1×1 unit cell indicated; scan area 4.7 nm $\times$ 4.7 nm.

dinated Sn atoms on the lower terrace of the steps for both step edge orientations. However, for the [010] step edges these fivefold coordinated Sn atoms are bonded to one twofold coordinated O atom. In other words, the same number of Sn to O bonds as O to Sn bonds were broken to form this step edge and therefore both O as well as Sn can maintain their oxidation state. For the [001] step edge this is not the case, only Sn to O bonds are broken and all oxygen atoms at the step edge are still fully threefold coordinated. Therefore the oxidation-state of the fivefold Sn atoms at the [001] step edge is *not* compensated, i.e., from a charge counting point of view the step-edge Sn atoms cannot attain a nominal 2+ or 4+ oxidation state if all the oxygen atoms are 2−. Consequently, most step edges of half a unit cell height are oriented along the [001] direction. One could even speculate that the elongated holes form by the decomposition, i.e., desorption of oxygen and tin from the surface layer at elevated temperatures, and that because of the unfavorable coordination of [001] step edges, this decomposition mainly propagates normal to this direction leaving elongated holes terminated by the more stable [010] steps.

The situation is different for steps of a full unit cell height (step I- type). The STM image reveals a clear predominance of step edges along the [001] direction, and indeed these are by far the lowest energy features on the reduced (100) surface found by our DFT calculations. The surface energy for this step edge at the UHV limit is -0.44 J/m^2, compared to 0.34 J/m^2 for the reduced (100) terrace, and hence will form spontaneously from a thermodynamic perspective. This step edge can be viewed as a (110) microfacet, i.e., a face identical to the lowest energy reduced (110) surface with both bridging and in-plane oxygens removed, as shown in Fig. 11(c). The unique feature of this step edge is that there are no "dangling" bonds if we accept that the surface prefers to be Sn^{2+}, i.e., all Sn and O atoms at the step edge have the same coordination as atoms on terraces. The fact that this step edge maintains a SnO stoichiometry rationalizes this favored step edge orientation. It also explains the experimental observation that full unit-cell height steps are observed along the [001] direction although half a unit cell step would give a similar terrace termination [see Fig. 11(b)].

The atomic corrugation on the terraces corresponds to the surface unit cell of $SnO_2(100)$-1×1. Figure 10(c) shows a row structure with the rows running along the direction of the close packed Sn atoms, i.e., the [001] direction. Figure 10(d) shows an atomically resolved STM image that allows clear discernment of the unit cell. The measured dimensions of the unit cell agree well with the dimensions of a 1×1 SnO_2 surface, i.e., 3.62 Å $\times$ 4.66 Å, thus indicating that the surface exhibits a bulk truncation.

2. $SnO_2(100)$: *Electronic structure*

The (100) surface converts from a stoichiometric 1×1 surface termination to a reduced 1×1 surface by removal of twofold coordinated bridging oxygen atoms under reducing conditions. The reduced (100) surface also attains a $Sn^{2+}O^{2-}$

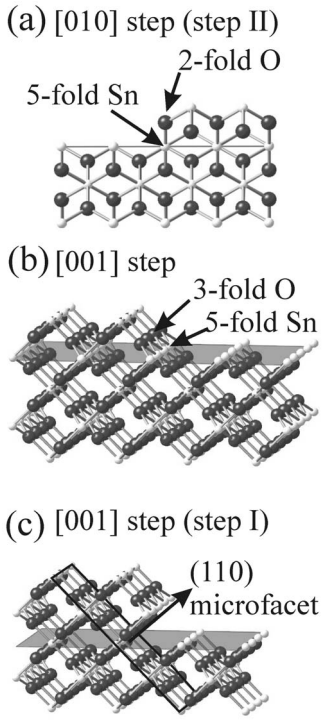

FIG. 11. Ball-and-stick model of step edges on the (100) surface. (a) Step edges oriented along the [010] crystallographic direction. Autocompensated step edges form for half-unit cell height step edges with fivefold coordinated Sn^{4+} and twofold coordinated O^{2-} atoms at the step edge. Models for step edges oriented along the [001] crystallographic direction are shown in (b) and (c). Half-unit cell height steps (b) are not autocompensated in this direction and therefore are not observed experimentally. Full-unit cell height steps (c) form (110) microfacets [identical to the reduced surface model shown in Fig. 4(b)] and therefore are energetically favored.

composition. As for the (101) surface, the reduced structures are formed after annealing in UHV and the stoichiometric surface termination is obtained by high-pressure oxygen treatment.

Figure 12(a) shows normal emission PES for the stoichiometric and reduced (100) surfaces at a photon energy of 26 eV. There is a pronounced increase in photoelectron emission for the reduced surface in the region of the valence band maximum. This additional state at the VBM for the reduced surface was observed for all photon energies investigated, i.e., in the range of 20 eV to 84 eV. This VBM state did *not* disperse with photon energy in normal emission spectra, implying that this is a surface state. Polarization-dependent photoemission studies verify the two-dimensional nature of this state. Figure 12(b) shows normal emission spectra for the same reduced (100) surface acquired with incident light at 70° and 40°, i.e., for *s* and *p* polarized light. For a 70° incidence angle with the vector potential **A** of the incident light almost normal to the sample surface, emission from the state at the VBM is almost completely suppressed, as is expected for a surface state. Thus a surface state exists at the VBM for the reduced (100) surface. Although we do not have resonant photoemission data for this surface to provide more direct evidence for the origin of this state, it is

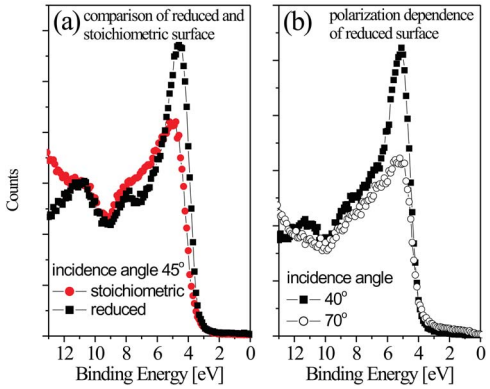

FIG. 12. (Color online) Normal-emission PES of the SnO_2(100) surface. (a) Comparison of photoemission from a stoichiometric (closed circles) and a reduced (black squares) surface, measured with a photon energy of 26 eV and a photon incidence angle of 45°. (b) Photoemission from a reduced surface with predominately *s*-polarized (open circles) and *p*-polarized (black squares) light.

reasonable to postulate that such a surface state would form from the filling of the Sn-5*s* states upon reduction of the surface atoms from Sn(IV) to a Sn(II).

C. SnO_2(101) surface

1. SnO_2(101)*: Composition and structure*

The structure and compositional changes of the (101) surface has been published in a previous paper.[69] Here we present a more detailed discussion of this surface in context with its electronic properties. Preparation of this surface by sputtering and annealing under UHV in a range of 600 K to 1000 K results in a 1×1 LEED pattern. In high-resolution STM images shown in Fig. 13(a) the unit cell of

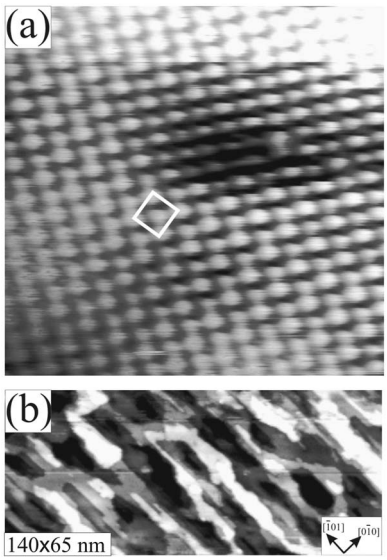

FIG. 13. STM images of the (101) surface. (a) Atomic resolution image with the unit cell indicated. (b) Large scale scan of 140 nm$\times$65 nm showing the high step edge density of this surface after vacuum preparation.

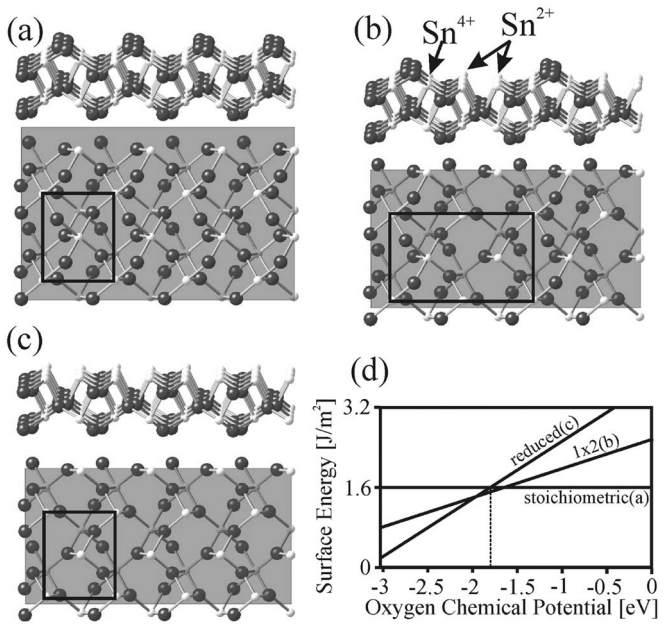

FIG. 14. Ball-and-stick models for different surface terminations of the (101) surface. (a) Stoichiometric, SnO_2, bulk termination. (b) A proposed 2×1 structure with every second bridging-oxygen row removed, leaving alternating double rows of Sn^{2+} and Sn^{4+}. (c) Surface layer with a SnO composition and with all surface-tin and oxygen atoms threefold coordinated. The dependence of the surface energy of these three models on the oxygen chemical potential is plotted in (c).

the (101) surface can be easily discerned. It consists of bright protrusions in the corner of a rectangle and a bright protrusion in its center. The center protrusion, however, appears to be asymmetric with respect to the symmetry axis of the rectangle described by the corner protrusions. The protrusions are consistent with positions of Sn atoms in an unreconstructed 1×1 bulk termination of the SnO_2(101) surface. The asymmetry of the center protrusion is due to the asymmetric coordination of the central Sn atom. These features are consistent with the SnO surface composition of the model reduced structure shown in Fig. 14(c). The calculated surface energy phase diagram shown in Fig. 14(d) indicates that under reducing conditions, this (1×1) reduced model is indeed the lowest energy surface structure.

Oxidation of the surface reveals considerable sensitivity of the resulting structure to experimental conditions. Exposure of the reduced (101) surface to 10 mbar O_2 does not result in a change of the qualitative 1×1 LEED pattern under most conditions. A few times, however, a 2×1 LEED pattern was observed, which converted to a 1×1 pattern upon vacuum annealing. Attempts to form this 2×1 pattern reproducibly were unsuccessful. These experimental results can be understood in terms of the calculated minimum free surface energy pathway from the reduced surface to the fully oxidized, stoichiometric structure. As can be seen in the surface free energy diagram in Fig. 14(d), the lowest energy structure under UHV, oxygen-poor conditions is the reduced structure in Fig. 14(c). As the oxygen chemical potential is increased (moving left to right), there is a very small region, from ~-2.0 to -1.7 eV, in which a (1×2) partially oxidized stoichiometry is lowest in energy. Above this region, the fully oxidized, stoichiometric (1×1) structure becomes the most stable under oxygen-rich conditions. In the (1×2) structure, every other row of Sn atoms has been oxidized from +2 to +4, as shown in Fig. 14(b). The narrowness of the region in which this (1×2) structure is the most stable is consistent with the experimental difficulty in obtaining it. Annealing this surface in vacuum will readily regenerate the (1×1) reduced structure. The atomic corrugation in STM images of the oxidized surfaces looks qualitatively the same as those for vacuum reduced surfaces. This can be understood if the contrast observed in empty-state STM images is dominated by Sn atoms for both oxidized and reduced surfaces. In LEIS the O/Sn ratio increases significantly after high-pressure oxygen exposure.

Figure 2(c) shows temperature dependent LEIS of an initially oxidized sample. An increase of the Sn peak is observed in a temperature range of 560–660 K. This indicates a depletion of oxygen atoms from the surface.

On vacuum prepared (101) surfaces a much higher step-edge density is observed compared to the (100) or the vacuum prepared (110) surfaces. Often very narrow terraces of only a couple of unit-cell widths are observed [see, e.g., Fig. 13(b)]. The preferential orientation of the step edges is along the [−101] direction. The high step edge density indicates a low formation energy for step edges.

2. SnO_2(101): *Electronic structure*

Secondary electron cutoff measurements show that the work function of the reduced (101) surface is ~1 eV lower than for the stoichiometric (101) surface. The experimental values for the reduced and stoichiometric surfaces are ~4.7 eV and ~5.7 eV, respectively. DFT calculations on the two fully relaxed surfaces are in good agreement with the experimental values. The theoretical values obtained for the reduced and stoichiometric surfaces are 4.7 eV and 6.1 eV, respectively. Such a pronounced difference in the work function is consistent with surfaces that exhibit two different bulk terminations with different oxygen contents. The somewhat lower experimental value for the stoichiometric surface compared to the DFT results may indicate the presence of oxygen vacancies at the surface, i.e., an incompletely oxidized surface.

Normal emission and angle-resolved photoemission data were collected on the VB for reduced and stoichiometric surfaces in order to identify surface states and characterize their band dispersion. These data are presented in the next two subsections. In Sec. III C 2 (3) the experimental results are compared with theoretical band structure calculations.

(1) Normal photoemission. Figure 15(a) shows normal emission PES for photon energies between 24 eV and 40 eV. The spectra were normalized to the integrated area of the photoemission intensity in the VB region with a binding energy between 0 eV and 12 eV. No compensation for the secondary electron background was made. The VB extends from 3.7 eV to 12.6 eV, thus we obtain a smaller width of the VB of 8.9 eV for this particular direction of the Brillouin zone than the previously reported value of ~10 eV for polycrys-

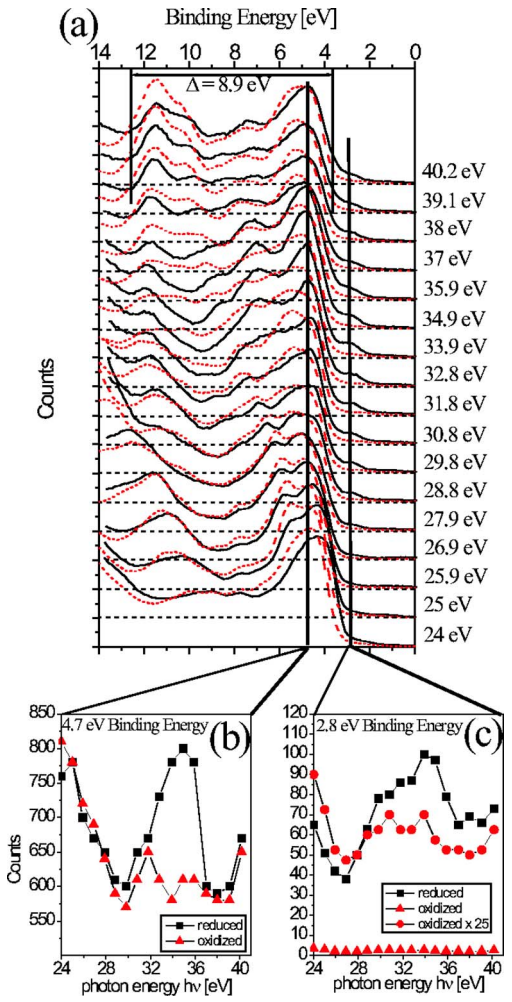

FIG. 15. (Color online) Dependence of valence band spectra of the SnO_2(101) surface on photon energy. (a) VB spectra for photon energies in a range of 24 eV to 40 eV for stoichiometric (dashed lines) and reduced (solid-black lines) surfaces. All spectra are normalized to the valence band area in a range of 0–12 eV binding energies. (b) Comparison of photoemission intensities for the reduced (black squares) and stoichiometric surface (triangles) at 4.7 eV binding energy. An increased photoemission intensity is observed for the reduced surfaces compared to the stoichiometric surface at photon energies between 30–36 eV. This is explained by a resonance with the Sn-4*d* core level. (c) Similar to (b) but for a binding energy of 2.8 eV.

talline SnO_2. The VB can be clearly divided into at least five sub-bands, which is more complex than the previous simplified division into O 2*p*, Sn 5*p*, and Sn 5*s* bands. Also, the bands show a clear dispersion with photon energy. It should be noted, however, that the (101) crystallographic direction is *not* a low symmetry direction of the bulk Brillouin zone. Thus no attempt has been made to characterize the dispersion of the bulk bands.

Comparison of the VB spectra of the reduced and stoichiometric SnO_2(101) surfaces show significant differences at the top of the VB. The reduced surface exhibits a state within the bulk band gap of SnO_2 that extends up to a binding energy of 2 eV with a maximum at ~2.8 eV. This band gap state does not disperse as a function of photon energy, which is indicative of a surface state. For the oxidized surface only a very small intensity is detected in this range. Additionally, there appears to be a higher photoemission intensity at a binding energy of ~4.7 eV at the VB maximum (VBM) for the reduced surface compared to the stoichiometric surface. Resonant photoemission has been used to identify the origin of the increased intensities for the reduced surface in the band gap and VBM regions. Figures 15(b) and 15(c) shows plots of the photoemission intensities at binding energies of 4.7 eV and 2.8 eV, respectively, as a function of photon energy. Increased photoemission is observed for photon energies between 30 eV and 36 eV for the reduced surface for both binding energies. The residual intensity in the band gap region at 2.8 eV for the stoichiometric surface also shows an increased intensity for the same photon energies [Fig. 15(c)], which suggests it is due to the same feature as the pronounced band gap state for the reduced surface.

The increased intensities at 30–36 eV can be explained by resonant photoemission of Sn-derived states as the photon energy is ramped through the threshold value for the dipole-allowed Sn $4d \Rightarrow$ Sn $5p$ transition [see Sec. III A 3 (2)]. Thus resonant PES indicates the presence of two Sn-derived surface states at the top of the VB for the reduced (101) surface, which are not present for the stoichiometric surface. Furthermore, the fact that the residual photoemission intensity in the band gap region shows the same behavior as the band gap state of the reduced surface implies that this intensity is due to oxygen vacancies at the surface, i.e., an incomplete oxidation of the surface during the sample preparation procedure.

(2) Surface band dispersion. In order to characterize the dispersion of the two surface states for the reduced SnO_2 (101) surface, angle-dependent PES were acquired along the Γ-X, Γ-Y, and Γ-M directions of the rectangular surface Brillouin zone. For comparison the same angle-resolved data were collected for the oxidized surface. This comparison of the two bulk terminations is made particularly easy in the case of SnO_2 (101) because both the stoichiometric and reduced surfaces have a 1×1 structure and thus share the same dimensions for the surface Brillouin zone. Figure 16 shows angle-resolved data along the three low symmetry directions for photon energies of 31.5 eV for the entire valence band region, and at 20 eV for the band gap region alone. PES for stoichiometric as well as for reduced surfaces are displayed. To guide the eye the position of the maxima of the surface states at the reduced surface are indicated in Fig. 16.

For surface states the momentum vector parallel to the surface ($k_{\|}$) is conserved in the photoemission process. The kinetic energy of the photoelectron defines the total momentum vector and the $k_{\|}$ component varies with the emission angle. Consequently, the emission angle can be related to a point in the surface Brillouin zone along the investigated azimuth direction according to the following relationship:

$$k_{\|} = (2m_e^* E_{\mathrm{kin}})^{1/2} 2\pi/h \sin\Theta, \qquad (1)$$

where Θ is the emission angle, m_e^* the effective electron mass, E_{kin} the kinetic energy of the photoelectron, and h is Planck's constant. Θ and E_{kin} are measured directly, but the effective electron mass must be estimated from the symmetry

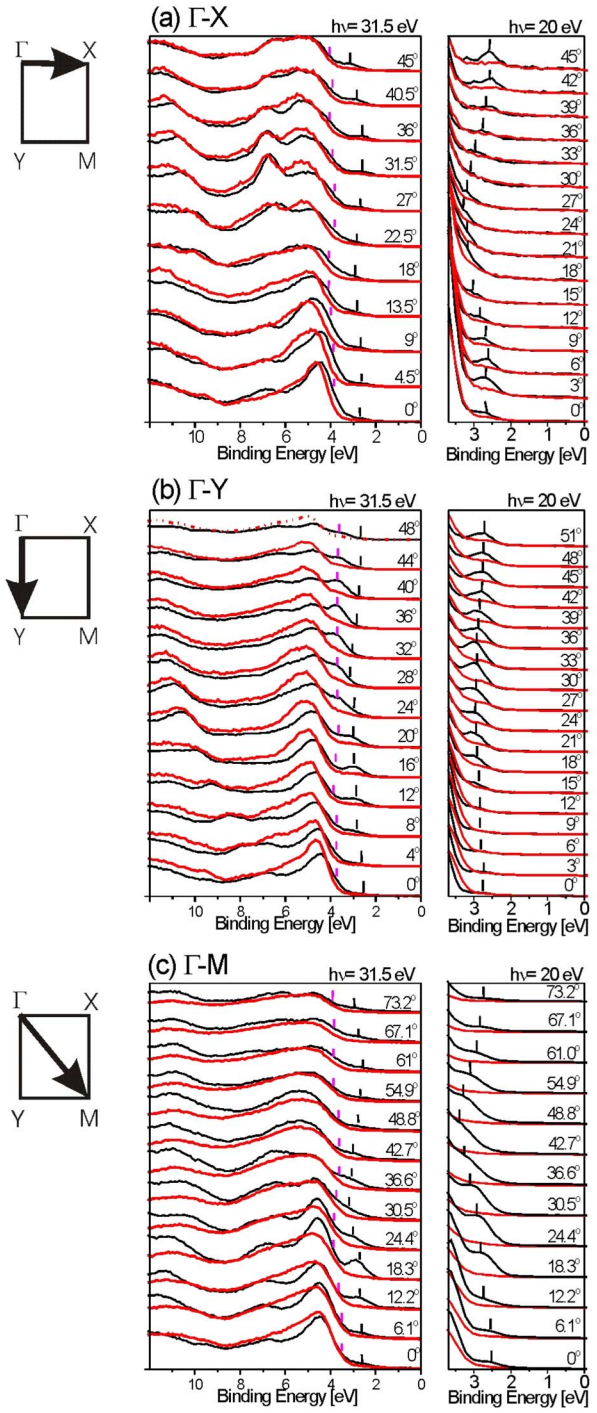

FIG. 16. (Color online) Angle resolved photoemission spectra for stoichiometric (gray lines) and reduced (black lines) $SnO_2(101)$ surfaces. The spectra were taken along low symmetry azimuth directions of the surface Brillouin zone as indicated on the left side: (a) Γ-*X*, (b) Γ-*Y*, and (c) Γ-*M*. The polar angles, measured from the surface normal, are indicated at each spectrum. Spectra for 31.5 eV (left panel) and 20 eV photon energy (right panel) are shown. The positions of the two identified surface states for the reduced surface are marked by black and gray dashes for each spectrum.

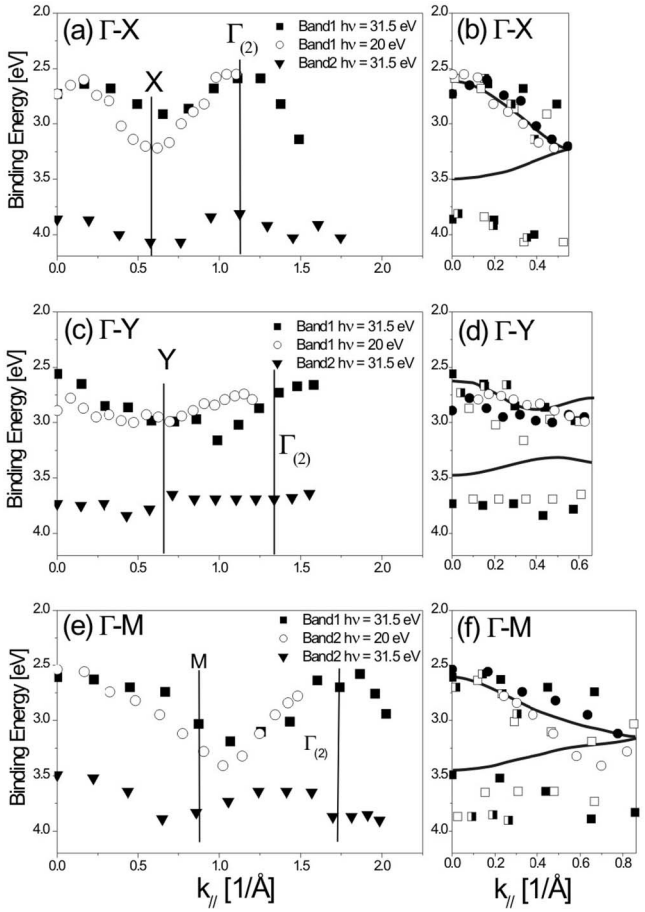

FIG. 17. Band dispersion of the surface states along (a) Γ-*X*, (c) Γ-*Y*, and (d) Γ-*M* directions of the reduced $SnO_2(101)$ surface deduced from the angle resolved PES shown in Fig. 2. The band dispersion was fitted to the symmetry points of the surface Brillouin zone by assuming an effective electron mass of 0.7 times the electron mass of a free electron. The same effective electron mass was used for all bands. (b), (d), and (f) show the reduced Brillouin zone scheme with all data points folded back into the first Brillouin zone. The solid lines represent calculated surface states (see Fig. 4).

of the band dispersion. The symmetry point of the band dispersion has to coincide with the Brillouin zone center or boundary. Thus the known dimensions of the surface Brillouin zone provide a fitting parameter for the effective electron mass. Figure 17 shows the band dispersion of the surface states obtained from the PES in Fig. 16. In order to fit the symmetry of the band dispersion to the Brillouin zone dimensions, an effective electron mass of 0.7 times the free electron mass was used. The right hand panel of Fig. 17 shows the reduced zone scheme with all the data points folded back into the first Brillouin zone for the three symmetry directions investigated.

(3) Comparison of experimental results with DFT calculations. Figures 18(a) and 18(b) show the electronic surface structure for the fully relaxed reduced and stoichiometric $SnO_2(101)$ surface structures, respectively. The binding energy in the calculations is referenced to the VBM, which is set to 0 eV. The bulk bands projected onto the (101) surface are indicated by the gray shaded area and surface states and

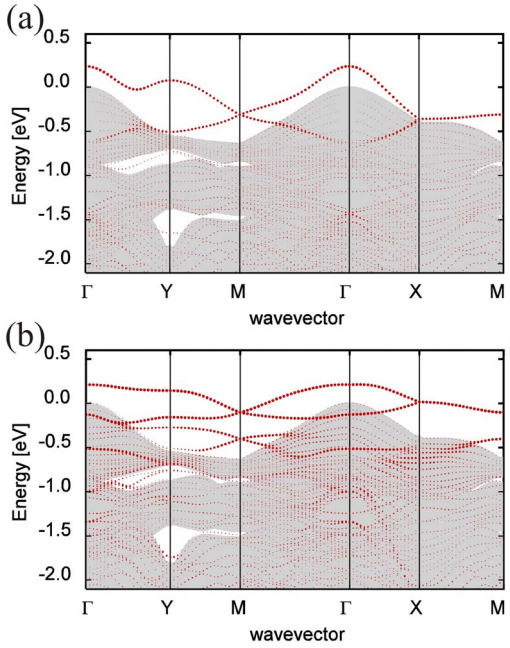

FIG. 18. (Color online) Band structure calculations for (a) the reduced and (b) the stoichiometric $SnO_2(101)$ surface. Gray shaded areas represent the projected bulk states; dots represent surface states and resonances.

resonances by the red dots. The calculated surface states for the reduced structure shown in Fig. 18(a) are in excellent agreement with the experimental results as indicated by the solid lines in the right hand panel of Fig. 17. The binding energies of the calculated bands are shifted in order to match the experimental data points, as the band gap is not accurately reproduced in DFT. The same shift has been used for all three symmetry directions. Agreement between theory and experiment for the second state is not as good as for the band gap state, which may be explained by difficulties in tracking this state in the experiments due to overlap with strong bulk states.

For the oxidized surface the calculations indicate surface states that are also distinct from the bulk VB, but only a weak emission was observed in the band gap region in the experiment, which was attributed to oxygen vacancies. Similar surface states within the band gap have been predicted for divalent bridging oxygen atoms for the (110) surface, but were also not observed [see Sec. III A 3 (2)].[35–37] These theoretically predicted states are due to the two lone pairs of the surface oxygen atoms, which are twofold coordinated. Unlike the Sn 5*s* states, these orbitals are highly localized and directional as in any typical tetrahedral, divalent oxygen molecule. From the molecular perspective, the oxygen valence shell is complete and is not undercoordinated. Because these orbitals are highly localized and directional, the photoemission may be highly angular dependent. This is in contrast to the metallic Sn 5*s* bands. Thus one may speculate that the predicted band gap states for the stoichiometric surface are not observed because of the symmetry of the wave function of the initial states. On the other hand, photoemission data were collected over a wide array of emission angles and no significant intensity in the band gap region was detected for any emission angle. This makes a highly angular dependent photoemission an unlikely reason for the lack of band gap states in the experimental studies. Another possible reason for the discrepancy between experiment and theory is that the complex sample preparation procedure of the stoichiometric surface may allow for contaminations, in particular hydrogen, and defects to be present at the surface. These deviations from a perfect stoichiometric surface may play a role in suppressing the predicted band gap states. Finally, the energy eigenvalues calculated by DFT for these lone pair states may simply be too high. In general strong surface states for stoichiometric oxide surfaces are very unusual.[70]

TABLE I. Calculated surface energies for fully relaxed *stoichiometric* (110), (100), and (101) surfaces.

	(110)	(100)	(101)
Surface energies $[J/m^2]$	1.21	1.29	1.60

IV. COMPARISON OF THE THREE LOW INDEX SURFACES

Ab initio atomistic thermodynamic calculations were performed to evaluate the surface energy of different surface structures as a function of the oxygen chemical potential. For all surface orientations studied the stoichiometric, i.e., SnO_2, bulk termination was the energetically favored surface only at high oxygen chemical potentials. The surface energies calculated for the fully relaxed stoichiometric surfaces are given in Table I. The same order for the surface energies of the three low index surfaces has been found as in previous calculations,[21–23] i.e., the surface energy increases in the order: (110), (100), and (101). At lower oxygen chemical potential, oxygen depleted surface phases become energetically favored. This is in agreement with the experimental LEIS studies that showed compositional transitions of the surfaces upon vacuum annealing. Plotting the surface energies for different surface compositions against the chemical potential allows a direct assessment of the thermodynamically favored surface structure at a given temperature and pressure, and a direct determination of the thermodynamic conditions at which a phase transition would be expected to occur.

The basic argument that surface structures that exhibit either a SnO or a SnO_2 composition are favored applies to the (100) and (101) surfaces. The difference between these surfaces and the (110) surface is that a conversion from a SnO_2 to a SnO surface layer can be readily accomplished by removal of the bridging oxygen (twofold coordinated surface oxygen) from the stoichiometric surface for the (100) and (101) surface, whereas on the (110) surface such a removal of bridging surface oxygen alone does not suffice to form a SnO surface layer. Additional in-plane oxygen atoms have to be removed from the (110) surface to obtain a surface layer that exhibits only Sn^{2+} surface atoms. This additional removal of some, but not all, in plane oxygen atoms is likely

TABLE II. Surface relaxations for stoichiometric and reduced (100) and (101) surfaces.

	(100)		(101)	
	Stoichiometric	Reduced	Stoichiometric	Reduced
D1-2	13.9%		13%	
D2-3	−6.9%	−6.3%	−13.4%	−4.5%
D3-4	24.6%	30.3%	12.7%	5.2%
D4-5	−3.7%	−3.1%	−9.6%	−0.2%
D5-6	−1.8%	−3.2%	1.3%	0.7%
D6-7	5.7%	8.9%	−0.2%	−1.1%
D7-8	−1.5%	−1.8%	0.4%	1.0%
D8-9	−0.3%	−0.4%		
D9-10	0.2%	0.09%		

responsible for the complex reconstructions and disorder observed on the (110) surface experimentally.

For the (100) and (101) orientations simple bulk terminations of the crystal exist that have surface tin atoms in either the 4+ or 2+ oxidation state. The absence of significant surface reconstructions has been verified experimentally by LEED and STM, which show the same unit cell for both the reduced and oxidized surfaces. Relaxation of the two surface terminations for the (100) and (101) surfaces have been calculated by DFT calculations. The vertical relaxations compared to the bulk planes are given in Table II. *Ab initio* atomistic thermodynamic calculations of fully relaxed surfaces confirm the experimental observation of a dual surface termination. Figures 14(c), 9(c), and 14(d) show that the oxygen rich surfaces are preferred at high oxygen chemical potential while the reduced surfaces become favored if the oxygen chemical potential is reduced. For the (101) surface an intermediate structure is found with a 2×1 superstructure consisting of alternating rows of bridging oxygen and rows with the bridging oxygen atoms removed, i.e., alternating double rows of Sn^{4+} and Sn^{2+} [Fig. 14(b)]. Such a structure has the lowest surface energy in a narrow range of oxygen chemical potentials and this is consistent with the infrequent observation of a 2×1 LEED pattern after high-pressure treatment. The phase transition chemical potentials can be read off in Figs. 4(c), 9(c), and 14(d). According to these figures the (101) surface reduces at somewhat higher chemical potential (−1.8 eV) than the (100) surface (−2.1 eV) but both surfaces reduce at higher oxygen chemical potentials than the (110) surface (−2.4 eV). At 10^{-14} mbar, chemical potentials of −1.76, −2.1, and −2.4 for the (101), (100), and (110) surfaces correspond to ~650 K, 765 K, and 865 K, respectively. Lower pressure would shift these threshold temperatures downward; higher pressure would increase them.

For all three low index surfaces investigated, Sn-derived surface states were identified for reduced surfaces with a $Sn^{2+}O^{2-}$ composition. Surface states for stoichiometric surfaces predicted by DFT calculations could not be detected experimentally.

It was hypothesized that the $Sn^{2+}O^{2-}$ composition of the reduced surfaces would exhibit electronic characteristics similar to that of tin monoxide with a Sn 5*s* derived state at a binding energy of ~2 eV. The greatest similarity was found for the reduced (110) surface with a Sn-derived state with a maximum at 2.5 eV and extending up to a binding energy of 2 eV. For the reduced (101) surface a band-gap state was also found but at slightly higher binding energies of ~2.8 eV. The (100) surface exhibited surface states close to the VBM of SnO_2. Thus the surface electronic structure clearly depends on the crystallographic face with surface states forming at different binding energies. Nevertheless for all three *reduced* surfaces, Sn-derived states were found at the top of the VB or within the bulk band gap of SnO_2 and thus show some analogy to the band structure of SnO.

V. DISCUSSION

One would hope that the experimentally measured transition temperatures can be related to the theoretically calculated transition oxygen chemical potentials. Setting the partial oxygen pressure in the vacuum chamber to 10^{-14} mbar, an extremely low but reasonable value for an UHV chamber, allows converting temperatures into chemical potentials because the chemical potential is a function of pressure and temperature only. Thus if the thermodynamic approach was valid the experimental values should be comparable to the theoretical ones. However, since low temperatures correspond to high chemical potentials at constant pressure, one can see at a glance that the experimentally measured trend in the reduction temperatures for the different surface orientations (see Fig. 2) is opposite to the one predicted by thermodynamics calculations. What impedes the thermodynamic description of the experiments is that no equilibration of the gas phase with the surface takes place at the time scales of the experiment. At these low pressures practically no oxygen reaches the surface from the gas phase and therefore it would take an extremely long time for the gas phase to equilibrate with the surface even in the absence of any kinetic barriers. This may be best illustrated by the fact that it would take of the order of 10^7 s for a monolayer of O_2 to reach the surface. Thus under the experimental conditions with annealing rates of 0.2 K/s the gas phase can be neglected. Consequently any transition temperatures observed must be governed by kinetics, i.e., activation barriers. Efforts for calculating kinetic barriers for O_2 desorption are currently underway. A consequence of the fact that under UHV conditions no equilibration with the gas phase can be obtained is that only kinetic barriers determine the surface phases that can be prepared. This means that intermediate phases thermodynamically favored for certain oxygen chemical potentials can only be obtained under UHV if they are also associated with a kinetic barrier preventing the formation of a lower energy surface at lower chemical potential. For instance this may explain why a $SnO_2(101)$-2×1 could not be prepared under UHV by annealing of a fully oxidized $SnO_2(101)$-1×1 surface, but instead the fully reduced surface is always obtained under UHV. Thus we conclude that in the experiments described here the activation barriers for desorption of oxygen from the surfaces is measured and not the thermodynamic equilibrium conditions. Thermodynamics may however be important un-

der realistic operation conditions at elevated pressures. Under such conditions the calculations show that the (101) surface reduces the easiest and the (110) surface stays stoichiometric for the longest if the oxygen chemical potential is reduced.

Surface reduction is not just limited to single crystal surfaces under UHV conditions but has also been observed for polycrystalline, sol gel-prepared SnO_2 gas-sensing materials upon exposure to reducing gases.[71] Thus the question is raised if changes in the electronic structure are contributing to the gas response signal in gas sensors and if so, which surface orientation contributes most. It is important to point out that although the (110)-4×1 reconstructed surface exhibits almost metallic properties and thus may be expected to influence the conductivity of gas-sensing materials significantly, this surface is *not* encountered in gas-sensing applications because it only forms after sputtering and annealing under UHV conditions. Nevertheless, the reduced (110)-1×1 surface exhibits the strongest surface states with the smallest band gap of the three low index surfaces investigated in this study. This implies that the (110) surface has potentially the largest impact on a surface-state-mediated gas response. However, all surface states observed on the reduced (110) and more so on the (101) and (100) surface are relatively low lying in the band gap region. Therefore it is not obvious that these surface states can impact the sample conductivity directly. It was previously speculated that electrons from surface states close to the Fermi edge could be injected into the bulk conduction band and thus contribute to the conductivity.[72] This hypothesis can be rejected because no surface states close to the Fermi edge were found in this study. It is more likely that a change in the conductivity for the reduced surface would be due to band bending induced by surface charges associated with the additional surface states. Charge neutrality is conserved by reducing the surface layer from $Sn^{4+}O_2^{2-}$ to $Sn^{2+}O^{2-}$, however, and no unambiguous indication of a band bending effect was found in the photoemission spectra. In any case, additional negative charges associated with the identified surface bands would cause an upward band bending and thus a reduced surface conductivity that is opposite to the measured gas response for SnO_2 gas sensors under reducing conditions. Thus we conclude that the surface states identified for the reduced surfaces do not directly contribute to the gas response. They may, however, play an indirect role because surface states are known to be important in the adsorption mechanism of molecules that ultimately trigger the gas response due to charge transfer from the SnO_2 surface to the adsorbate. The importance of the surface termination on the interaction with gas phase molecules has been recently demonstrated for water adsorption on reduced and stoichiometric SnO_2(101) surfaces. It was found that water dissociatively adsorbs on the reduced surface but only interacts weakly with the oxidized surface.[73]

Finally, surface states are also important in (opto)electronic devices that use SnO_2 as a transparent electrode material. If used as an electrode these surface or interface states may influence the charge transfer across the interface. The presence and possible control of these surface states by oxidation or reduction during processing provides a valuable guide for device fabrication.[74] Furthermore, the strong changes and degradation of the band gap that is encountered on the (110) surface may make this crystallographic orientation of SnO_2 an undesirable interface for electronic applications.

VI. CONCLUSIONS

Compositional changes at surfaces of SnO_2 are facilitated by the dual valency of Sn. This results in surfaces dominated by a stable SnO or SnO_2 composition. The rutile structure of SnO_2 easily facilitates formation of SnO and SnO_2 compositions for bulk terminations of the (100) and (101). We found experimentally and theoretically that these are indeed the preferred surface terminations and that a phase transition from one surface termination to the other occurs with a variation of the oxygen chemical potential. For the (110) surface the lowest surface energy structure at the UHV limit was also found to be SnO with bridging and in-plane oxygen rows removed. The complex surface structures observed on the (110) surface make it a difficult surface for fundamental studies and it appears that the (100) and (101) surfaces are much better suited in this respect. The dependence of the surface composition on the oxygen chemical potential of the system and thus the gas phase properties was quantified by *ab initio* thermodynamics calculations. These calculations verified the tendency of SnO_2 to form a reduced SnO surface layer at low oxygen chemical potential. The possibility to prepare unreconstructed (100) and (101) surfaces with either a tin or oxygen termination will allow probing the dependence of interface properties of SnO_2 on its surface composition in future studies.[73,74]

Electronic structure measurements showed that all reduced SnO_2 surfaces exhibit surface states due to the filling of Sn-5*s* states upon reduction of surface Sn atoms from Sn^{4+} to Sn^{2+}. These states are observed at the top of the VB or fairly deep within the bulk band gap of SnO_2.

ACKNOWLEDGMENTS

The authors thank Dr. Yaroslav Losovyi for assistance in performing the photoemission experiments and Professor R. Helbig for the generous donation of the SnO_2 single crystals. Acknowledgment is made to the Donors of the American Chemical Society Petroleum Research Fund, to the NSF (Grant No. CHE-0109804), and NASA for financial support.

[1] H. C. Yao and Y. Yao, J. Catal. **86**, 254 (1984).
[2] C. Agrafiotis, A. Tsetsekou, and A. Ekonomakou, J. Mater. Sci. Lett. **18**, 1421 (1999).
[3] L. G. Appel, J. G. Eon, and M. Schmal, Catal. Lett. **56**, 199 (1998).
[4] G. Centi, in *Catalysis from A to Z*, edited by B. Cornils, W. A. Hermann, R. Schlögel, and C.-H. Wong (Wiley-VCH, Weinheim, 2000).
[5] C. Stampfl, M. V. Ganduglia-Pirovano, K. Reuter, and M. Scheffler, Surf. Sci. **500**, 368 (2002).
[6] K. Reuter and M. Scheffler, Phys. Rev. B **68**, 045407 (2003).
[7] N. Barsan and U. Weimar, J. Electroceram. **7**, 143 (2001).
[8] N. Barsan, M. Schweizer-Berberich, and W. Göpel, Fresenius' J. Anal. Chem. **365**, 287 (1999).
[9] C. Malagù, V. Guidi, M. Stefancich, M. C. Carotta, and G. Martinelli, J. Appl. Phys. **91**, 808 (2002).
[10] V. Lantto, T. T. Rantala, and T. S. Rantala, J. Eur. Ceram. Soc. **21**, 1961 (2001).
[11] N. Barsan and U. Weimar, J. Phys.: Condens. Matter **15**, R813 (2003).
[12] E. de Frésart, J. Darville, and J. M. Gilles, Appl. Surf. Sci. **11/12**, 637 (1982).
[13] J. W. Erickson and S. Semancik, Surf. Sci. Lett. **187**, L658 (1987).
[14] M. Egashira and Y. Shimizu, in *Chemical Sensor Technology, Volume 3*, edited by N. Yamazoe (Elsevier Science, Amsterdam, 1991).
[15] E. Comini, G. Faglia, G. Sberveglieri, Z. Pan, and Z. L. Wang, Appl. Phys. Lett. **81**, 1896 (2002).
[16] P. G. Harrison, C. Bailey, and W. Azelee, J. Catal. **186**, 147 (1999).
[17] P. W. Park, H. H. Kung, D.-W. Kim, and M. C. Kung, J. Catal. **184**, 440 (1999).
[18] T. J. Coutts, D. L. Young, and X. Li, MRS Bull. **25**, 58 (2000).
[19] M. Batzill and U. Diebold (unpublished).
[20] B. Thiel and R. Helbig, J. Cryst. Growth **32**, 259 (1976).
[21] A. Beltrán, J. Andrés, E. Longo, and E. R. Leite, Appl. Phys. Lett. **83**, 635 (2003).
[22] J. Oviedo and M. J. Gillan, Surf. Sci. **463**, 93 (2000).
[23] B. Salter, C. R. Catlow, D. H. Gay, D. E. Williams, and V. Dusastre, J. Phys. Chem. B **103**, 10644 (1999).
[24] W. Bergermayer and I. Tanaka, Appl. Phys. Lett. **84**, 909 (2004).
[25] M. Batzill, K. Katsiev, and U. Diebold, Surf. Sci. **529**, 295 (2003).
[26] D. F. Cox, T. B. Fryberger, and S. Semancik, Phys. Rev. B **38**, 2072 (1988).
[27] Z. S. Li, Q. L. Guo, and P. J. Møller, Z. Phys. D: At., Mol. Clusters **40**, 550 (1997).
[28] V. A. Gercher, D. F. Cox, and J.-M. Themlin, Surf. Sci. **306**, 279 (1994).
[29] V. A. Gercher and D. F. Cox, Surf. Sci. **332**, 177 (1995).
[30] R. Cavicchi, V. Sukkarev, and S. Semancik, J. Vac. Sci. Technol. A **8**, 2347 (1990).
[31] S. Munnix and M. Schmeits, Phys. Rev. B **27**, 7624 (1983).
[32] J. M. Themlin, R. Sporken, J. Darville, R. Caudano, J. M. Gilles, and R. L. Johnson, Phys. Rev. B **42**, 11914 (1990).
[33] J.-M. Themlin, M. Chtaïb, L. Henrard, P. Lambin, J. Darville, and J.-M. Gilles, Phys. Rev. B **46**, 2460 (1992).
[34] V. M. Jiménez, G. Lassaletta, A. Fernández, J. P. Espinós, F. Yubero, A. R. González-Elipe, L. Soriano, J. M. Sanz, and D. A. Papaconstantopoulos, Phys. Rev. B **60**, 11171 (1999).
[35] J. Oviedo and M. J. Gillan, Surf. Sci. **467**, 35 (2000).
[36] M. A. Mäki-Jaskari and T. T. Rantala, Phys. Rev. B **64**, 075407 (2001).
[37] T. T. Rantala, T. S. Rantala, and V. Lantto, Mater. Sci. Semicond. Process. **3**, 103 (2000).
[38] T. J. Godin and J. P. LaFemina, Phys. Rev. B **47**, 6518 (1993).
[39] I. Manassidis, J. Goniakowski, L. N. Kantorovich, and M. J. Gillan, Surf. Sci. **339**, 258 (1995).
[40] M. A. Mäki-Jaskari and T. T. Rantala, Phys. Rev. B **65**, 245428 (2002).
[41] R. G. Egdell, J. Rebane, T. J. Walker, and D. S. L. Law, Phys. Rev. B **59**, 1792 (1999).
[42] M. Sinner-Hettenbach, M. Göthelid, T. Weiß, N. Barsan, U. Weimar, H. von Schenck, L. Giovanelli, and G. Le Lay, Surf. Sci. **499**, 85 (2002).
[43] D. F. Cox, T. B. Fryberger, and S. Semancik, J. Vac. Sci. Technol. A **6**, 828 (1988).
[44] Cerambond 865, Aremco-products, Inc.
[45] P. A. Dowben, D. LaGraffe, and M. Onellion, J. Phys.: Condens. Matter **1**, 6571 (1989).
[46] J. P. Perdew, K. Burke, and M. Ernzerhof, Phys. Rev. Lett. **77**, 3865 (1996).
[47] B. Delley, J. Chem. Phys. **92**, 508 (1990).
[48] B. Delley, J. Chem. Phys. **113**, 7756 (2000).
[49] K. Reuter and M. Scheffler, Phys. Rev. B **65**, 035406 (2002).
[50] X. G. Wang, A. Chaka, and M. Scheffler, Phys. Rev. Lett. **84**, 3650 (2000).
[51] Q. Sun, K. Reuter, and M. Scheffler, Phys. Rev. B **67**, 205424 (2003).
[52] K. Reuter and M. Scheffler, Phys. Rev. Lett. **90**, 046103 (2003).
[53] W. X. Li, C. Stampfl, and M. Scheffler, Phys. Rev. B **68**, 165412 (2003).
[54] X.-G. Wang, W. Weiss, Sh. K. Shaikhutdinov, M. Ritter, M. Petersen, F. Wagner, R. Schlögl, and M. Scheffler, Phys. Rev. Lett. **81**, 1038 (1998).
[55] M. W. Chase, NIST-JANAF Thermochemical Tables, 4th ed. [J. Phys. Chem. Ref. Data (1998)].
[56] L. V. Gurvich, I. V. Veyts, and C. B. Alcock, *Thermodynamic Properties of Individual Substances*, 4th ed. (Hemisphere Publishing Corporation, New York, 1991), Vol. 2.
[57] B. Delley, Int. J. Quantum Chem. **69**, 423 (1998).
[58] I. Vaquila, J. W. Rabalais, J. Wolfgang, and P. Nordlander, Surf. Sci. **489**, L561 (2001).
[59] C. E. Sosolik, J. R. Hampton, A. C. Lavery, B. H. Cooper, and J. B. Marston, Phys. Rev. Lett. **90**, 013201 (2003).
[60] R. J. A. van den Oetelaar and C. F. J. Flipse, Phys. Rev. B **52**, 10807 (1995).
[61] C. L. Pang, S. A. Haycock, H. Raza, P. J. Møller, and G. Thornton, Phys. Rev. B **62**, R7775 (2000).
[62] R. A. Bennett, P. Stone, N. J. Price, and M. Bowker, Phys. Rev. Lett. **82**, 3831 (1999).
[63] M. Li, L. Groß, W. Hebenstreit, U. Diebold, M. A. Henderson, D. R. Jennison, P. A. Schulz, and M. P. Sears, Surf. Sci. **437**, 173 (1999).
[64] F. H. Jones, R. Dixon, J. S. Foord, R. G. Egdell, and J. B. Pethica, Surf. Sci. **376**, 367 (1997).
[65] A. Atrei, E. Zanazzi, U. Bardi, and G. Rovida, Surf. Sci. **475**, L223 (2001).
[66] H. Onishi and Y. Iwasawa, Phys. Rev. Lett. **76**, 791 (1996).

[67] P. W. Murray, N. G. Condon, and G. Thornton, Phys. Rev. B **51**, 10989 (1995).
[68] J.-M. Thelmin, J.-M. Gilles, and R. L. Johnson, J. Phys. IV **C9**, 183 (1994).
[69] M. Batzill, A. Chaka, and U. Diebold, Europhys. Lett. **65**, 61 (2004).
[70] U. Diebold, Surf. Sci. Rep. **48**, 53 (2003).
[71] C. Canevali, N. Chiodini, P. Di Nola, F. Morazzoni, R. Scotti, and C. L. Bianchi, J. Mater. Chem. **7**, 997 (1997).
[72] V. Lantto, T. T. Rantala, and T. S. Rantala, J. Eur. Ceram. Soc. **21**, 1961 (2001).
[73] M. Batzill, W. Bergermayer, I. Tanaka, and U. Diebold (unpublished).
[74] M. Batzill, K. Katsiev, and U. Diebold, Appl. Phys. Lett. **85**, 5766 (2004).